Type I X-ray bursts in GS 1826-24

Michael Zamfir

Master of Science

Department of Physics

McGill University

Montreal, QC, H3A 2T8, Canada

2010-06-21

A thesis submitted to McGill University in partial fulfilment of the requirements of the degree of Master of Science

ACKNOWLEDGEMENTS

I wish to acknowledge my supervisor, Andrew Cumming, to whom I am indebted for his guidance, support, and above all, his patience and willingness to help. He has made this work possible in so many ways, and I thank him sincerely.

I also wish to thank my family, in particular my parents, who have always supported me in the pursuit of my goals.

ABSTRACT

Type I X-ray bursts in low-mass X-ray binaries are well understood to be due to thermonuclear flashes from accreting neutron stars. Previous work on the modeling of bursts from GS 1826-24 has had good results in reproducing the main bursting characteristics, particularly the lightcurves. We show that with a simple model for a spreading burning front, we are able to build on those previous results and improve the agreement in the lightcurves as well as find good agreement with the evolution of the burst spectrum. We also investigate the decrease in inferred emission area observed in bursts from this same source at very late times during the bursts. We show that with a very simple model for Comptonization of a blackbody spectrum, we were able to reproduce, and thus provide a possible explanation for, the observed behaviour of the spectrum.

ABRÉGÉ

Nous démontrons qu'avec un simple modèle de propagation du front d'une explosion en rayons X, nous pouvons bien reproduire par simulations le flux et le spèctre observés pendant les premiers instants d'explosions provenant de la source GS 1826-24. Nous démontrons aussi qu'avec un simple modèle de Comptonisation d'un spèctre de corps noir, nous pouvons reproduire, and ainsi possiblement expliquer l'observation de la baisse de l'aire d'émission déduite pendant la fin des explosions.

TABLE OF CONTENTS

CHAPTER 1
Introduction

Many accreting neutron stars in low mass X-ray binaries exhibit bright momentary flashes in X-rays from unstable nuclear reactions on their surfaces. These events which occur every few hours or days are known as Type I X-ray bursts, or simply X-ray bursts.

The study of X-ray bursts is important for a number of reasons. It can reveal clues into the nuclear physics which power the bursts, including some poorly known reaction rates and β-decay lifetimes. Knowledge of the nuclear processes taking place on the NS surface is key to understanding the composition in the layers beneath, in the crust, which is made up of the ashes of nuclear burning. X-ray bursts can also be used to measure the neutron star (NS) spin, mass, and radius, as these parameters influence the burst spectral and timing properties. Measurements of the mass and radius of neutron stars are very important as they can help us discriminate between NS equations of state, and thus give us an insight into the behaviour of matter at supranuclear densities. Finally, measurements of the distance can also be done with X-ray bursts, typically with those whose surface flux reaches the Eddington limit, and thus behave as a standard candle.

In this work, we studied X-ray bursts from GS 1826-24. In Chapter 2, we attempt to model the early parts of the observed bursts using a parametrized model which simulates a spreading burning front rapidly engulfing the NS surface. In Chapter 3, we look at the latter parts of the burst spectrum which show a behaviour unexpected given the assumption of the NS surface emitting roughly as a blackbody. We show that using a model

where burst emission, initally assumed to be Planckian, is Comptonized in a plasma, we can adequately reproduce the observed behaviour.

In the following sections, we will cover some of the background topics necessary to put our work into context.

1.1 *Neutron stars*

The existence of compact stars made of neutrons had been speculated as early as 1934, by Baade and Zwicky, as the result of core-collapse supernova [Baade and Zwicky, 1934]. The first discovery of a neutron star came about in 1967 when Anthony Hewish and his then graduate student Jocelyn Bell Burnell discovered regular radio pulsations from what is known today as a pulsar, which is a rapidly rotating, highly magnetized NS.

Neutron stars are compact stellar objects containing matter at and above nuclear densities in their interiors. At the densities and pressures present in the NS interior, it becomes energetically favorable for protons and electrons to form free neutrons. While free neutrons normally β decay in about 15 minutes, at sufficient depths in the NS the decay reaction is suppressed as the Fermi energy becomes too high to be populated by the electrons which would be created in the decay. Neutron stars are supported by the degeneracy pressure of those free neutrons, as is the case of white dwarfs with electrons, but there are also nuclear interactions which play a very important role in the pressure balance.

They are formed as remnants of evolved massive (8-20$M_\odot$) stars which have undergone core collapse. They will typically have a mass of around $1.4M_\odot$ and a radius of $\sim$ 10 km. Conserving the angular momentum of its predecessor but with a much smaller moment of inertia, the NS can have spin periods which vary from 30 s or longer to approximately 1.4 ms [Hessels

et al., 2006]. It is believed that the fastest rotating NSs have been spun up by accretion in a binary (more on this in the following section).

1.2 *Low-mass X-ray binaries*

The term Low-mass X-ray binary (LMXB) generally refers to a binary system consisting of a compact object, either a NS or black hole, orbiting a low-mass ($\lesssim 1.4 M_\odot$) star, typically on the Main Sequence, but also possibly in more advanced evolutionary stages. In such a binary system, the equipotential surface around a star delimiting the space within which matter is bound to that star is called its *Roche lobe*. See Figure 1–1 for an illustration of the Roche potential.

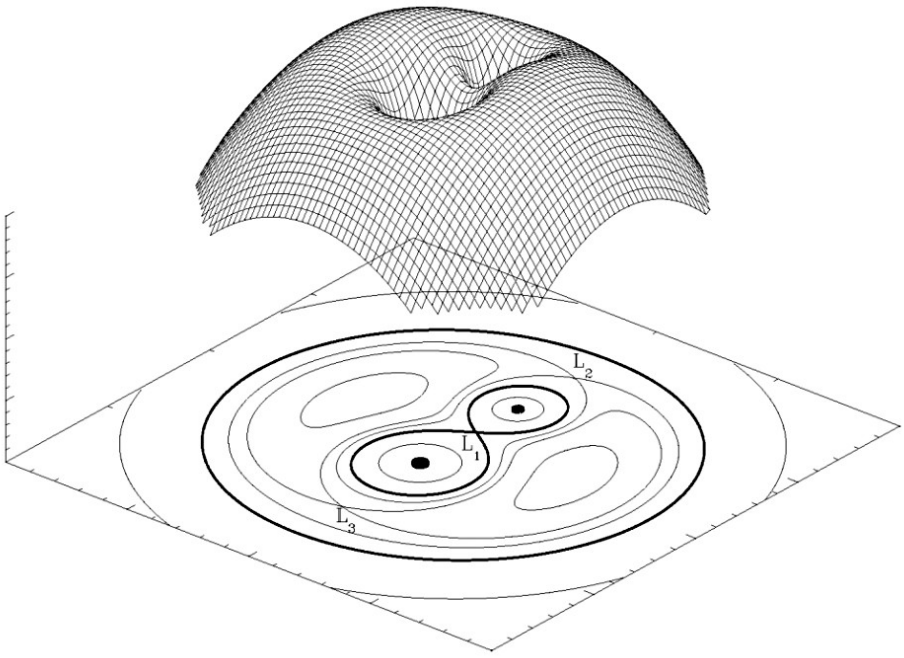

Figure 1–1: A plot of the Roche potential, with a projection onto the plane below. The Roche lobe has a tear-drop shape with the tips meeting at the L_1 Lagrange point, which is the point of equilibrium for the gravitational pulls of the two binary objects. [source: *http://hemel.waarnemen.com/Informatie/Sterren/hoofdstuk6.html*]

In a LMXB, the low-mass companion, or donor, will fill its Roche lobe. The L_1 point, being a saddle point, serves as a "pass" between the two Roche lobes, so that mass which finds itself slightly outside of one lobe will eventually make its way into the other lobe via L_1. The mass which makes its way through L_1 will appear, from the compact star's perspective, as though it were being squirted out of a nozzle which is rotating around it at the orbital period, in the orbital plane. The incoming mass thus possesses angular momentum from the orbital motion and it will begin to orbit the compact object, eventually forming an accretion disk. Angular momentum in the disk is transported outward (see Papaloizou and Lin [1995] for a review of the possible mechanisms at work in this process) and mass progresses inward (see Frank et al. [1985] or later editions for a treatment of accretion).

During accretion, a substantial amount of angular momentum can be acquired by the NS, from the orbit of the binary. In this manner, a NS can be spun up to very short periods. It is the accepted evolutionary scenario that NSs in LMXBs eventually become millisecond pulsars after the accretion phase, when the companion has either collapsed into a degenerate white dwarf, or perhaps been destroyed, either by X-ray irradation from the NS during accretion, or from a pulsar wind of relativistic particles (see Tauris and van den Heuvel [2003] and references therein).

Eventually this mass, which, originating typically from the surface of a Main Sequence star, is made up of mostly light elements, will accrete down onto the surface of the NS (henceforth an LMXB will be assumed to have a NS as its compact object). Inferred accretion rates in LMXBs are around $10^{-10} - 10^{-8} M_\odot\,\mathrm{yr}^{-1}$. Using the canonical values for NS mass and radius of $1.4 M_\odot$ and 10km, respectively, this gives a gravitational energy release of

approximately

$$L \approx \frac{GM_{NS}\dot{M}}{R_{NS}} \approx 10^{36} - 10^{38}\,\mathrm{ergs/s}. \tag{1.1}$$

Assuming that the accreted mass thermalizes once it reaches the surface of the NS, with the gravitational energy eventually being re-emitted from the whole NS surface as a blackbody, we can estimate the temperature as

$$Flux \approx \frac{10^{36} - 10^{38}\,\mathrm{ergs/s}}{4\pi R_{NS}^2} \approx \sigma T^4 \tag{1.2}$$

which gives a surface temperature of

$$k_B T \approx 0.5 - 1.6\,\mathrm{keV}. \tag{1.3}$$

As of 2007, there were a total of 183 known LMXBs, 84 of which have exhibited bursts [Liu et al., 2007].

1.3 *Type I X-ray bursts*

As we saw in the previous section, LMXBs can emit X-rays simply from gravitational energy release. In many of these systems, however, energetic events occur which amplify temporarily the X-ray flux by 1 or 2 orders of magnitude. Type I X-ray bursts are characterized by a rapid rise in flux lasting 1 to 5 seconds, followed by an exponential-like decay lasting from 10 to 100 seconds (see Figure 1–2). They release around $10^{39} - 10^{40}$ergs of energy of nuclear origin, and occur with periods ranging from hours to roughly one day.

The energy release from nuclear burning of a solar mixture to heavy elements is $\sim 5\,\mathrm{MeV}$ per nucleon, compared to $GM/r \approx 200\,\mathrm{MeV}$ per nucleon in gravitational energy. This may seem astonishing given the brightness of X-ray bursts, and indeed if the nuclear and gravitational energies were released at the same rate, evidence for nuclear reactions would

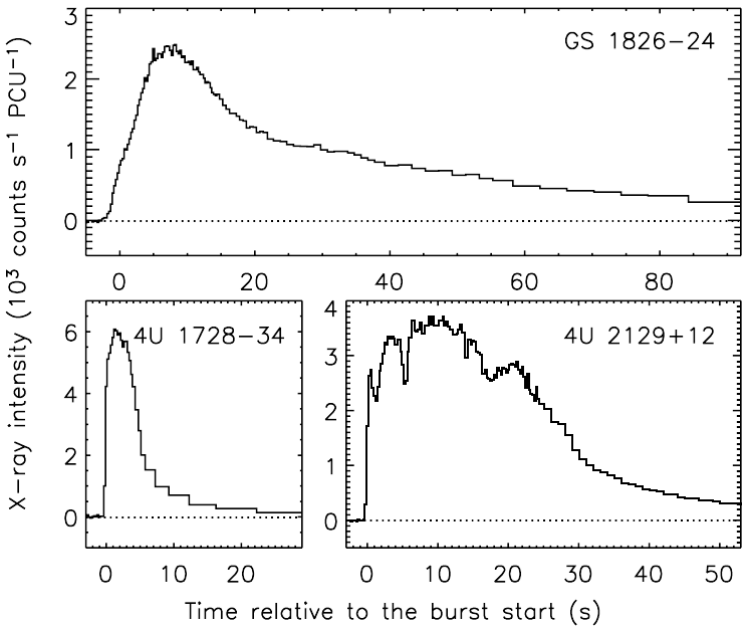

Figure 1–2: Lightcurves of X-ray bursts of differing shapes. [Galloway et al., 2008]

be very difficult to detect. As such, the only way to see the clear signs of nuclear burning is for the fuel to accumulate for a period of time, and then release all or part of its nuclear energy rapidly.

X-ray bursts are indeed theoretically well understood to be caused by such unstable burning of light elements which accrete for hours or days. A layer of hydrogen and helium-rich matter accumulates near the surface of the NS, eventually undergoing thermal runaway via the *thin-shell instability*. This process was first discovered in theory by Schwarzschild and Härm [1965] in the helium layer residing above the carbon/oxygen core of evolved $1\,M_\odot$ stars. If a shell in hydrostatic balance is sufficiently thin, heating it will not change the pressure at its location, which is dictated by the weight of the matter sitting on top of it. If in this shell the nuclear heating rate becomes more temperature sensitive than the cooling rate, then it can be shown that any temperature perturbation will cause thermal runaway, leading to a rapid nuclear burning of the accreted fuel layer. This is the

accepted mechanism for the unstable burning which powers X-ray bursts, with either hydrogen or helium burning driving the instability.

During a burst, hydrogen will be consumed via the CNO or *hot* CNO cycles (CNO standing for carbon, nitrogen and oxygen), and helium via the triple-α reaction.

The triple-α reaction occurs in two phases. Firstly, two α particles will bind to make ^{8}Be, which is unstable and has a lifetime of only 2.6×10^{-16} s [Clayton, 1968]. At high temperatures ($\gtrsim 10^8$ K), the production of ^{8}Be will be fast enough to create a sufficient amount of ^{8}Be for the second phase of the reaction to occur; $^8\mathrm{Be}(\alpha,\gamma)^{12}\mathrm{C}^\star$, where $^{12}\mathrm{C}^\star$ is an excited state of ^{12}C. $^{12}\mathrm{C}^\star$ will either decay back into ^{8}Be and an alpha particle or emit a γ-ray and settle to the ground state ^{12}C.

The reaction rate of the triple-α reaction would be extremely small if not for the existence of a particular resonant reaction energy. In the second part of the reaction, ^{8}Be+α has almost the same energy as $^{12}\mathrm{C}^\star$. In fact, from the study of relative abundance of ^{12}C in stellar atmospheres, Fred Hoyle notably predicted the existence of this excited state, permitting the resonance which greatly amplifies the production of ^{12}C [Hoyle, 1954].

The CNO cycle turns hydrogen into helium. It requires the presence of carbon, usually produced in the triple-α reaction, but no carbon is in fact consumed; it only acts as a catalyst. The main branch of the the regular (or *cold*, as we shall refer to it) CNO cycle is as follows [Hansen et al., 2004]:

$$
\begin{aligned}
^{12}\mathrm{C} + ^1\mathrm{H} &\longrightarrow {}^{13}\mathrm{N} + \gamma \\
{}^{13}\mathrm{N} &\longrightarrow {}^{13}\mathrm{C} + \mathrm{e}^+ + \nu_e \\
^{13}\mathrm{C} + ^1\mathrm{H} &\longrightarrow {}^{14}\mathrm{N} + \gamma
\end{aligned}
$$

$$
\begin{aligned}
{}^{14}\mathrm{N} + {}^{1}\mathrm{H} &\longrightarrow {}^{15}\mathrm{O} + \gamma \\
{}^{15}\mathrm{O} &\longrightarrow {}^{15}\mathrm{N} + \mathrm{e}^{+} + \nu_e \\
{}^{15}\mathrm{N} + {}^{1}\mathrm{H} &\longrightarrow {}^{12}\mathrm{C} + {}^{4}\mathrm{He}
\end{aligned}
$$

The main branch of the *hot* CNO cycle is the following [Wiescher et al., 2010]:

$$
\begin{aligned}
{}^{12}\mathrm{C} + {}^{1}\mathrm{H} &\longrightarrow {}^{13}\mathrm{N} + \gamma \\
{}^{13}\mathrm{N} + {}^{1}\mathrm{H} &\longrightarrow {}^{14}\mathrm{O} + \gamma \\
{}^{14}\mathrm{O} &\longrightarrow {}^{14}\mathrm{N} + \mathrm{e}^{+} + \nu_e \\
{}^{14}\mathrm{N} + {}^{1}\mathrm{H} &\longrightarrow {}^{15}\mathrm{O} + \gamma \\
{}^{15}\mathrm{O} &\longrightarrow {}^{15}\mathrm{N} + \mathrm{e}^{+} + \nu_e \\
{}^{15}\mathrm{N} + {}^{1}\mathrm{H} &\longrightarrow {}^{12}\mathrm{C} + {}^{4}\mathrm{He}
\end{aligned}
$$

The distinction between the two is that during the hot CNO cycle, which occurs at a higher temperature, ^{13}N, before having time to β-decay down into ^{13}C, will capture a proton and thus branch off from the regular CNO cycle. The temperature at which the hot CNO cycle begins to operate is $\simeq 8 \times 10^7$K.

The regular CNO cycle is temperature sensitive, since an increase in temperature will speed up the proton-captures and make duration of the cycle shorter, thus increasing the rate of energy production. In the hot CNO cycle, however, the proton captures already happen almost instantaneously, and thus the only events which set the timescale for the cycle duration are the two β-decays in the 3^{rd} and 5^{th} lines. Therefore, within the range of temperatures at which the hot CNO cycle operates, the energy production is constant, and independent of temperature. However, at temperatures

above $\sim 10^9$ K, hydrogen burning will break out from the hot CNO cycle via rapid-proton captures, also known as the *rp*-process.

The *rp*-process in an X-ray burst begins after helium burning has produced carbon and increased the overall temperature. The process itself consists of successive proton captures onto the ashes of burnt helium as well as β-decays. The β-decay rates are what limits the energy release rate in this process. The *rp*-process produces progressively heavier elements, up to Tellurium ($Z = 52$) [Schatz et al., 2001]. Because of the β-decays, the rp-process is expected to release energy for 10-100 seconds after the burst has initiated, presumably producing longer duration bursts (see the first burst profile in Figure 1–2).

While helium burning can occur very rapidly, the burning of hydrogen via the CNO cycles or the *rp*-process is relatively slow, as it limited by the necessary β decays within those reactions.

As we mentioned before, either hydrogen or helium can drive the instability which leads to an X-ray burst. For hydrogen to ignite the layer, it must be burning via the cold CNO cycle, which has a temperature dependence in the rate of proton captures. The *hot* CNO cycle is thermally *stable*, as it does not respond to changes in the temperature (assuming the temperature remains in the range for *hot* CNO burning) and thus cannot drive the thin-shell instability. For accretion rates of $\dot{M} \lesssim 0.01\dot{M}_{Edd}$ (where we take the Eddington accretion rate to be $\dot{M}_{Edd} = 1.7 \times 10^{-8} M_\odot\,\mathrm{yr}^{-1}$), the temperature in the accreting layer will be $T \lesssim 8 \times 10^7$ K [Cumming, 2004], hydrogen burning will be in the cold CNO cycle regime whose instability will lead to "hydrogen-triggered" bursts.

If the accretion rate is larger than $\dot{M} \approx 0.01\dot{M}_{Edd}$, the temperature in the accreting layer will be raised above 8×10^7 K and hydrogen will

burn stably on a timescale of ∼1 day (for solar metallicity) [Bildsten, 2000]. Helium burning will drive the instability in this case, and there are two possibilities for the burst regime, depending on whether there is hydrogen left in the layer (since it burns continuously) at ignition. If there is little or no hydrogen left in the accreting layer, there will be a "pure He" burst, whereas the presence of hydrogen in the accreted layer will give a *mixed H/He* burst. Pure He bursts are very short and energetic, as helium burning occurs very rapidly. Photospheric radius expansion bursts, where the surface flux exceeds the Eddington limit and thus blows the photosphere outwards, are attributed to pure helium bursts. Mixed H/He bursts, with their long durations are associated with hydrogen burning via the *rp*-process, as we mentioned before.

At accretion rates approaching $\dot{M} \approx \dot{M}_{Edd}$, the temperature in the accreted layer will be $T \approx 5 \times 10^8$ K [Cumming, 2004] and the temperature sensitivity of the triple-α reaction will be less than that of the cooling. Both hydrogen and helium will then burn stably and no bursts should occur.

1.4 *GS 1826-24*

GS 1826-24 (also known as Ginga 1826-238) is a transient source known for both its frequent and unusually regular, both in periodicity and shape, bursts (see figure 1–3 for 20 of its burst profiles). It was first discovered by *Ginga*, a Japanese X-ray telescope in 1988 [Tanaka, 1989]. The detection of thermonuclear bursts with *BeppoSAX* enabled Ubertini et al. [1997] to affirm the presence of a NS in this system. During 2.5 years of subsequent observations with *BeppoSAX*, Ubertini et al. [1999] found a recurrence time of 5.76 ± 0.62 hours, dubbing this source a "clocked thermonuclear flash generator" for its high regularity. Bildsten [1998] suggested that this source

exhibits bursts which are a "textbook" case for the mixed H/He regime. Heger et al. [2007] confirmed that assertion by showing that by modeling the bursts with a careful treatment of the *rp*-process, they were able to very closely reproduce all the main features of X-ray bursts from this source, including the $\sim$ 5 s rise time and 100 s cooling tail (see figure 1–4 for a plot of their best fit model, A3, against an average observed burst profile). In their models, they did however find a two-stage rise during the burst onset which is not seen in the observations. In the next chapter, we attempt to resolve the discrepancy during the burst onset by developing a simple spreading model.

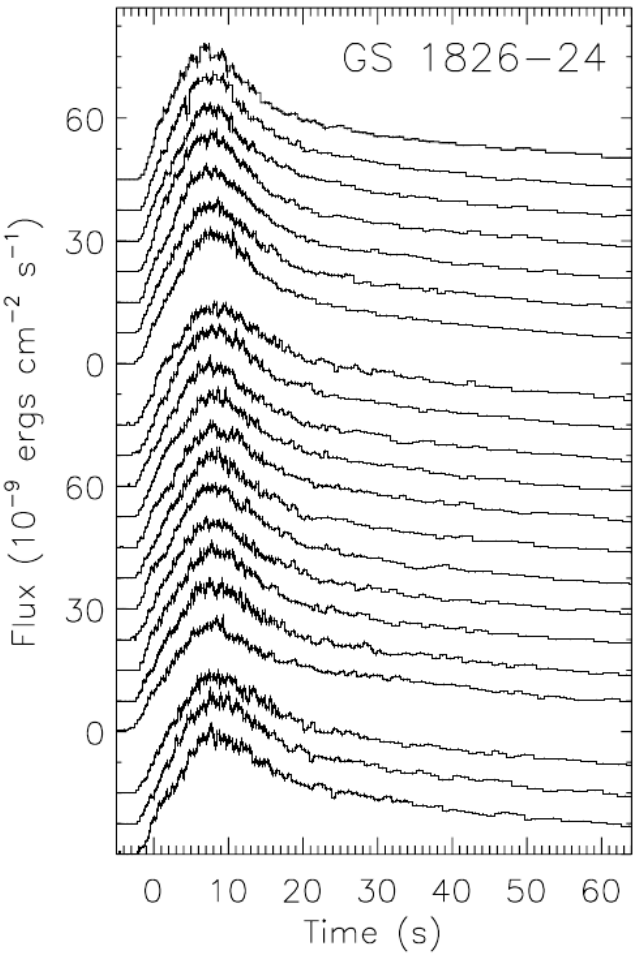

Figure 1–3: The profiles of 20 X-ray bursts observed with RXTE between 1997 and 2002, plotted with a vertical offset [Galloway et al., 2004].

in't Zand et al. [2009] also looked at bursts from GS 1826-24, focusing on the detection of hour-long cooling tails. They found that using the same multizone calculation presented in Heger et al. [2007] as the most agreeable fit to the bursts (model A3), they were able to explain these very long tails as the delayed cooling of deep layers (up to $\sim$ 10 times deeper in column density than the ignition location) which, due to the energy released in the rapid burning of the nuclear fuel powering the bursts, are heated by inward conduction.

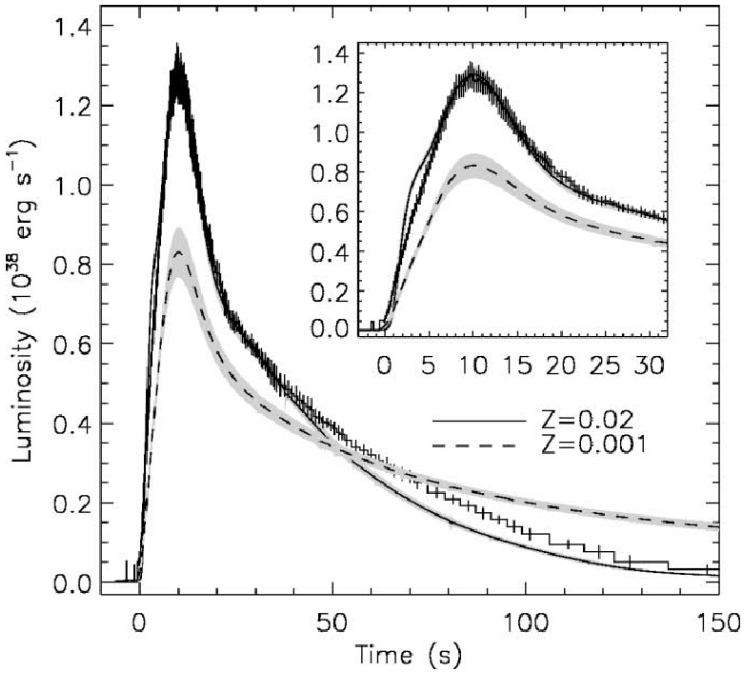

Figure 1–4: A comparison of an average observed lightcurve, represented by the histogram (from bursts observed by RXTE in 2000), with two burst models with different metallicities for the accreted material. Model A3 is represented by the black solid curve (with $Z = 0.02$). The inset plot is a magnification of the early portion of the burst [Heger et al., 2007].

in't Zand et al. [2009] also discuss a peculiar feature of the time-resolved photometric data, which shows a sudden drop off in inferred emission area in bursts from GS 1826-24, as well as other sources (see the 3$^{\rm rd}$ panel from the top in figure 1.4). The expectation, assuming neutron

star emission is that of a blackbody, would be to see a constant inferred emission area, with a decreasing temperature. They could not find a definite explanation for this behaviour, but did suggest two possibilities. Firstly, this could be an effect associated with the procedure with which burst spectra are processed, namely by the subtraction of the pre-burst emission from the total emission during the burst (see van Paradijs and Lewin [1986]). Secondly, it could be the effect of Comptonization of the neutron star emission by a hot plasma. This unresolved topic will be adressed in Chapter 3.

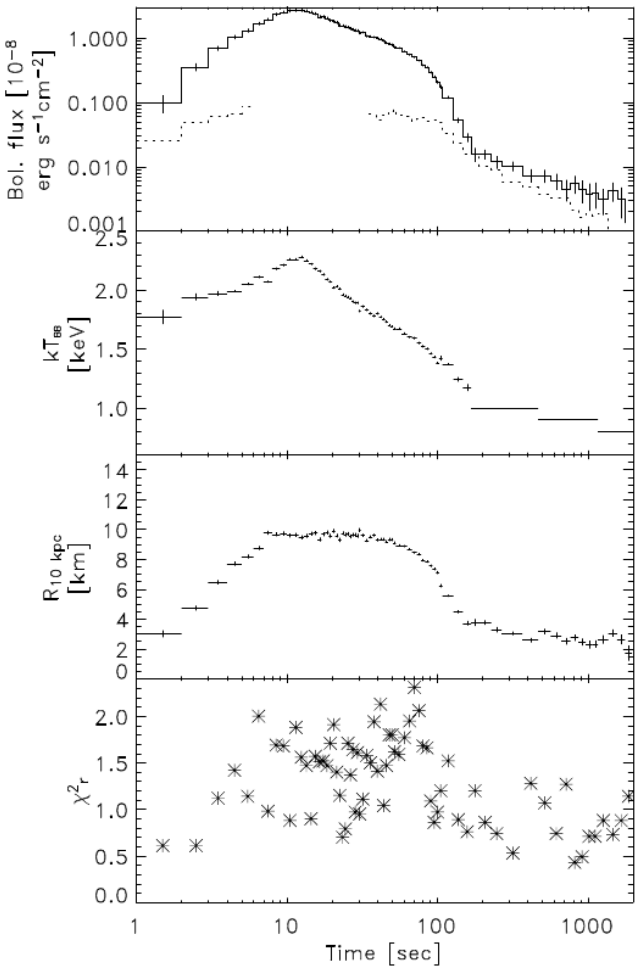

Figure 1–5: Plots showing the time-resolved photometric data of an average of 17 bursts from GS 1826-24, observed with RXTE. The top panel shows a plot of the bolometric flux as a solid curve, the second panel shows a plot of the (fitted) blackbody temperature, the third panel the blackbody radius at a distance of 10 kpc (1 kpc= 3.08568×10^{19} m), and the bottom panel shows the goodness-of-fit of the blackbody spectrum to the burst emission in terms of the reduced χ^2. [in't Zand et al., 2009]

CHAPTER 2
Superficial spreading in Type I X-ray bursts from GS 1826-24

2.1 *Observations and theory of spreading*

It has long been expected that bursts must be initiated at a single location on the star, and then presumably a burning front would spread outwards, igniting the neighbouring regions, eventually engulfing the whole surface. Shara [1982] first put forth this idea, by arguing that the accretion timescale, which is comparable to the time it takes to reach unstable burning conditions in the accreted layer, is much longer than the timescale for burning of the nuclear fuel.

Observational evidence supporting the interpretation that ignition occurs as a progressively expanding *hot spot* comes from analyzing burst spectra. By fitting a blackbody to the emission during the early stages of an X-ray burst from 4U 1728-34, Strohmayer et al. [1997] generated a plot of the quartic root of effective emitting area ($A^{1/4}$) against the total flux (the vertical and horizontal axes in Figure 2–1, respectively) with time as a parameter, for one burst. What is clearly visible is that at early times, the emitting area was smallest, then growing with the increasing flux during the rising stage of the burst. After the peak flux is reached, the inferred emitting area stays roughly constant for the remainder of the burst duration, while the flux declines, suggestive of a radiating NS surface which is cooling.

Highly coherent oscillations which are detected in some bursts during the rise phase are interpreted as the spin-modulated emission from a

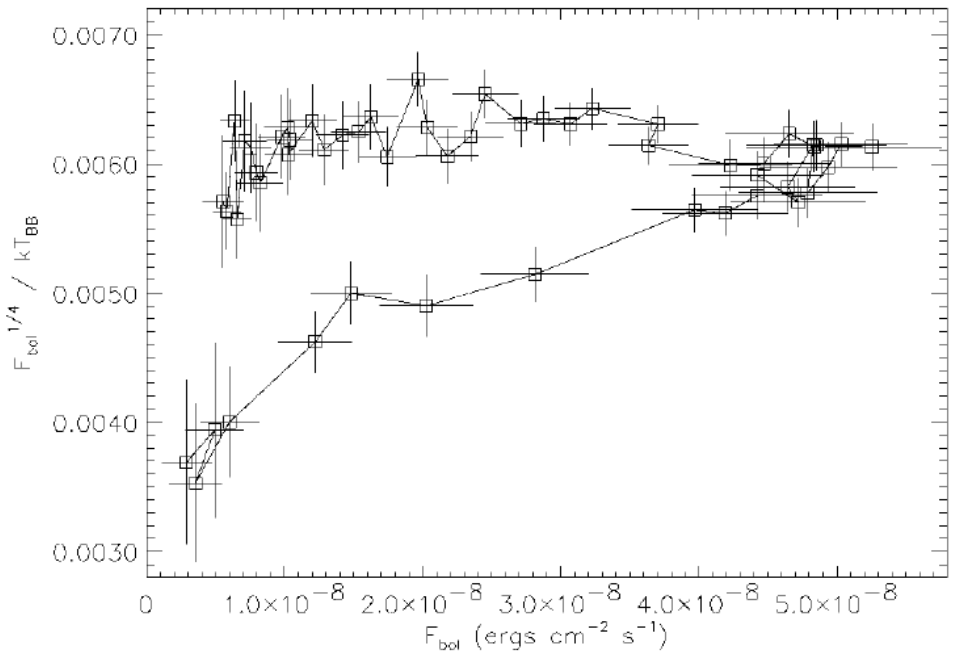

Figure 2–1: A plot of the quartic root of effective emitting area ($A^{1/4}$) against the total flux shown on the the vertical and horizontal axes, respectively, with time as a parameter for a burst from 4U 1728-34. (Note: $t = 0$ corresponds to a point at the *bottom left* of the plot, while the end of the burst ($t = t_f$) is at the *top left* of the plot) [Strohmayer et al., 1997].

growing hot spot. Particularly telling are studies of the time-resolved amplitudes of these burst rise oscillations. Figure 2–2 shows the large initial amplitude in the burst-rise oscillation from 4U 1728-34, suggestive of a hot spot ignition. Presumably, the large amplitudes are due to the initially small hot spot which becomes occulted as the NS spins around. The oscillation amplitude then diminishes as the hot spot grows, its radiation becoming visible to a distant observer during all phases of the spin period.

Theoretical models suggest that ignition should in most cases occur on the equator. Assuming that the surface layers of the spinning NS prior to ignition are in hydrostatic equilibrium and are at rest in the corotating frame, the arguments of Spitkovsky et al. [2002] for equatorial ignition are as follows (see also Cooper and Narayan [2007]). Presuming that the accreted matter distributes itself on the surface in such a way as to minimize

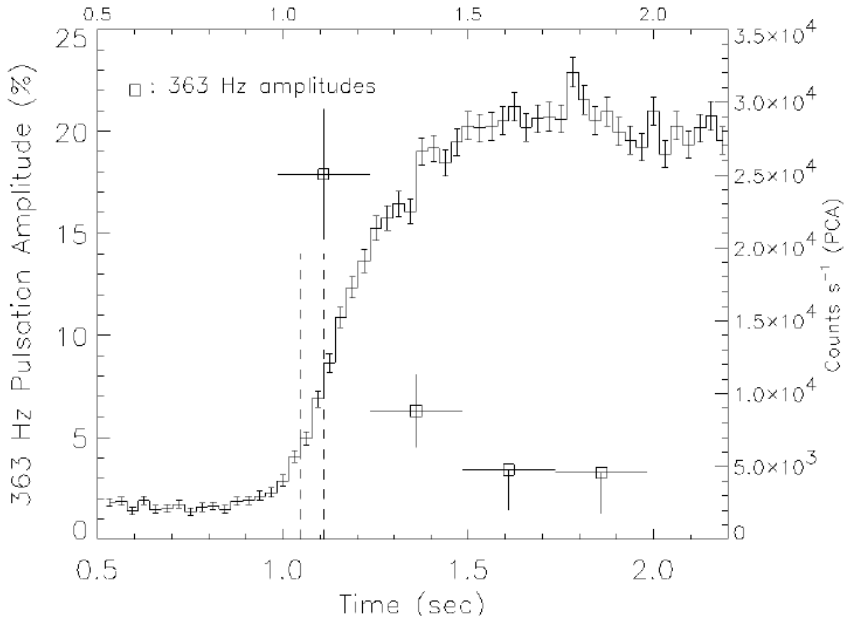

Figure 2–2: Evolution of the oscillation amplitude during the rise of a burst from 4U 1728-34 [Strohmayer et al., 1997].

its potential energy, the base of the accreted layer will be an equipotential surface. This implies that the pressure at the base of the accreted ocean is the same everywhere:

$$p_{base} = g_{eff}(\lambda) y_{base}(\lambda) = \text{constant} \tag{2.1}$$

where $g_{eff}(\lambda)$ is the effective gravitational acceleration, $y_{base}(\lambda)$ is the column depth[1] at the base of the accreted layer and λ the latitude. Therefore, $y_{base} \propto 1/g_{eff}$ and taking the time derivative of Equation 2.1, we also get that $\dot{y} \propto 1/g_{eff}$ [2] , where $\dot{y}$ is the local mass accretion rate. From Equation

[1] defined as $y = \int \rho dz$, where ρ is the mass density, and z the spacial coordinate which increases with depth into the star.

[2] since p_{base} increases as more material is piled onto the star surface through accretion, and thus has a time-dependence.

(20) in Bildsten [1998], the column depth at which Helium ignites scales as

$$y_{ign} \propto \dot{y}^{-1/5} g_{eff}^{-2/5} \tag{2.2}$$

To obtain an ignition timescale as a function of the latitude, we combine the last equation with $\dot{y} \propto 1/g_{eff}$ to get

$$t_{ign}(\lambda) \equiv \frac{y_{ign}}{\dot{y}} \propto \dot{y}^{-1/5} g_{eff}^{3/5} \propto g_{eff}^{4/5} \tag{2.3}$$

Since the NS is spinning rapidly (typically at rates upwards of 300 Hz), the centrifugal acceleration lessens g_{eff}, and thus t_{ign}, such that they are both a minumum at the equator. This implies that ignition should occur preferentially at the equator.

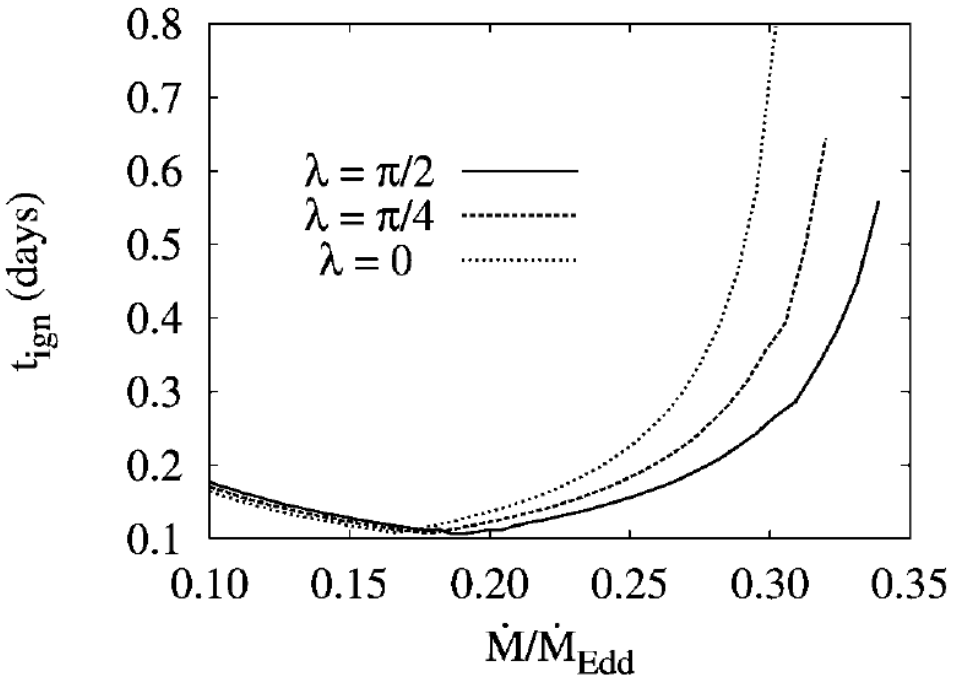

Figure 2–3: Plot showing t_{ign} for 3 latitudes ($\lambda = 0$ at the equator, $\lambda = \pi/4$, and $\lambda = \pi/2$ at the pole) as a function of the accretion rate. Note the reversal at $\dot{M} \approx 0.17\dot{M}_{Edd}$, beyond which ignitions preferably near the poles [Cooper and Narayan, 2007].

Cooper and Narayan [2007] agree with the conclusions of Spitkovsky et al. [2002] for low accretion rates, but argue that beyond a critical

accretion rate, ignition will preferentially occur away from the equator. The argument is based on theoretical and observational evidence that as the accretion rate increases, bursting regimes change (see §1.3), eventually bursts being quenched altogether at a high enough accretion rate, as the nuclear fuel burns stably. They show that there is a range of accretion rates where the regions near the equator will have moved into the regime of"delayed mixed bursts" (see Cooper and Narayan [2006] for more on this), which are bursts occuring with higher recurrence times, while the regions closer to the poles would still exhibit shorter recurrence bursting behaviour. As such any ignition would preferentially occur in regions away from the equator. See Figure 2–3 from Cooper and Narayan [2007], where they have plotted t_{ign} for 3 latitudes as a function of the accretion rate. Note that the location with the shortest ignition time turns over at $\dot{M} \approx 0.17\dot{M}_{Edd}$ from being at the equator to being at the pole. At high enough accretion rates $\dot{M} \gtrsim 0.3\dot{M}_{Edd}$, nuclear burning becomes stable at the equator (indicated by the asymptotic rise of the t_{igm} timescale in Figure 2–3), remaining unstable at latitudes nearer to the pole, thereby in theory eliminating any possibility for ignition on the equator. It should be noted that according to their stability analysis, bursts from GS 1826-24 should ignite preferentially at the equator, since its accretion rate is believed to be $\dot{M} \approx 0.07\dot{M}_{Edd}$ [Galloway et al., 2004].

2.2 *A simple model of spreading*

To understand what effects a burning spreading front might have on the X-ray burst lightcurve and spectrum, we developed a simple model for the spreading process after ignition. We ran parametrized simulations to

generate lightcurves and spectra, eventually comparing our models to observations. Our model has three main components. Firstly, a time-dependent, local surface flux profile for ignited regions on the NS surface. Second, we employed three spreading velocity models, defining the propagation of the burning front. Finally, our model has a lightcurve and spectral time-series generating routine, which takes into account the curved trajectories of light in the vicinity of the NS.

The model depends on three physical parameters: the gravitational redshift z at the NS surface relative to a distant inertial observer, the inclination (or obervation angle) i with respect to the star's rotation axis, and the spreading time t_s, that is, the time it takes for the burning front to engulf the star surface.

In our model, the ignition occurs everywhere on the equator at once, and spreads uniformly towards the poles. We divided the NS surface into 800 patches by creating a grid of points at equal azimuthal and polar angles from each other. The largest grid cells had an area of ~ 2.4 km^2. We found that this was sufficiently small, although we did run simulations with a finer grid, to ensure that we had not lost any accuracy by enlarging the grid. We determined the emission of the partially ignited grid cells (those which the front has reached, but not crossed) by linearly interpolating the flux based on the fraction of the cell area that was ignited. Once a patch was ignited, the flux it emitted was given by model A3 from Heger et al. [2007] (see figure 1–4). To generate a spectrum, we assumed that every grid cell emitted as a blackbody with a local temperature derived from the local flux via the Stefan-Boltzmann law. Grid cells yet to be ignited were assumed to have no flux, or a temperature $T = 0$ K. (See Appendix A for an analytical and simplified version of the lightcurve generating model without relativistic

effects, a simple instant-rise and exponential decay local flux and with a constant burning front speed.)

As we mentioned previously, Heger et al. [2007] made models of X-ray bursts, with comparisons to burst data from GS 1826-24. They used a 1-dimensional (in depth) hydrodynamics multizone model to simulate sequences of bursts with the accretion rate and accretion composition as the main parameters. Their code was equipped with a nuclear reaction network for energy generation, in particular useful in its ability to track the *rp*-process in detail (see Woosley et al. [2004]). Since the code is 1-dimensional, the resulting emission was assumed to be uniform across the whole star surface. As we mentioned before, Heger et al. [2007] show that their model, with an appropriately chosen accretion rate and composition (corresponding to the model they referred to as A3), reproduces all the main features of X-ray burst luminosities from GS 1826-24, namely a slow ($\sim$ 5 s) rise with a long ($\sim$ 100 s) tail, a burst recurrence time of around 4 hours, and a burst profile which mostly agrees well with the observed one. They do however find disagreement in the burst rise where their model has a two-stage rise, which is not seen in the observations. We used model A3 as our local flux because it is a model which appears to best reflect the main bursting characteristics of this source, as well as one we felt we could improve in terms of agreement with observations by including it in a simple spreading scheme.

To model the spreading of the ignition front, we utilized expressions for the burning front speeds v_{flame} derived in Spitkovsky et al. [2002]. They argued that during a burst which ignites locally, the layer of the NS which has ignited becomes very hot ($\sim 2 \times 10^9$K) and thus its scaleheight increases, raising the hot ocean by 10 to 40 m relative to a cold, unignited

region of the star surface. This creates a horizontal pressure gradient which increases with height, driving a shear flow and circulation across the burst front. Since the NS is rotating rapidly, away from the equator there is a Coriolis force along the direction of the front line (and perpendicular to the horizontal pressure gradient) due to the horizontal flow across the front. In this system, the flow due to the Coriolis force, known as the geostrophic flow, dominates the *ageostrophic* flow across the front. This effectively slows the propagation of the burst front, particularly as the front moves towards the rotational poles, where the strength of the Coriolis force is greater.

Our model design is based on this idea, as well as the results of Cooper and Narayan [2007] suggesting equatorial ignition. Since a burst front would not be subject to the Coriolis force at the equator, one would expect it move very rapidly in the lateral directions, tracing out an ignition "belt" around the NS equator. As the burst front would then spread towards the pole, it would be slowed by the process described in the previous paragraph.

The expression for v_{flame} Spitkovsky et al. [2002] obtain, which depends on a number of parameters, including the timescale for unstable nuclear burning during the burst t_n, as well as the unknown timescale for frictional coupling between the top and the bottom of the hot ocean t_{fr}, is given by

$$v_{flame} \sim \left[\frac{g h_{hot}}{t_n} \frac{1/t_{fr} + \eta/t_n}{f^2 + (1/t_{fr} + \eta/t_n)^2} \right]^{1/2} \tag{2.4}$$

The dependence of the front speed on the polar angle θ is expressed through the Coriolis parameter $f = 2\Omega \cos\theta$, where Ω is the angular frequency of the star spin. g and h_{hot} are the surface gravity and scaleheight of the hot ocean, respectively, and η is a number of order unity.

In the limit of weak frictional coupling (i.e. $t_{fr} \gg t_n$ and $t_{fr} \gg 1/f$), the spreading speed becomes

$$v_{flame} \sim \left[\frac{g h_{hot}}{t_n} \frac{\eta/t_n}{f^2 + (\eta/t_n)^2} \right]^{1/2} \tag{2.5}$$

Since typical spin frequencies of bursting NSs in LMXBs are upwards of 300 Hz, giving $f \approx 2000$, and the nuclear timescale t_n for helium burning via the triple-α reaction is ~ 0.1 s for temperatures of $\sim 2 \times 10^9$ K, the above equation can be further reduced to

$$v_{flame} \propto \frac{1}{\cos\theta} \tag{2.6}$$

We are mainly interested in how the speed scales with latitude. Its magnitude is parametrized in our model as the spreading time t_s.

If friction is important (i.e. $t_{fr} \lesssim t_n$), then the resulting speed will depend on how t_{fr} compares to $1/f$. Spitkovsky et al. [2002] show that the front speed in this regime attains a maximum when friction is acting on the rotation timescale, that is $1/t_{fr} = f$, and this turns expression 2.4 into

$$v_{flame}^{max} \sim \left(\frac{g h_{hot}}{f t_n} \right)^{1/2} \tag{2.7}$$

or simply

$$v_{flame}^{max} \propto \frac{1}{\sqrt{\cos\theta}} \tag{2.8}$$

For this spreading speed regime to be sustained throughout the burst, $1/t_{fr}$ would need to have the same latitude dependence as f, to preserve the $1/t_{fr} = f$ condition.

Lastly, if f is small compared to $1/t_{fr}$ either because of high friction or because the star rotates slowly, then v_{flame} will have no θ-dependence. In other words, the front will propagate at a constant speed. In this case,

it would not be expected that the burst front would develop into a belt-like shape, as we modeled it, since the Coriolis force would no longer be a dominant force in the ignition propagation mechanism. As such, the burst would be expected to grow circularly until it engulfed the whole star surface. We ignored this caveat in our simulations, and assumed that such a burst would still spread uniformly outwards from the equator in a belt-like shape, for purposes of comparison.

Simulations with all three burst front latitudinal dependencies (or *speed regimes*) were done in an attempt to find, by comparing lightcurves and spectral time-series to observations, some indication of the validity of the different speed regimes.

To get an expression for the latitude reached by the front as a function of time, as we required to run our simulations, we needed to integrate the expressions for burning front speed regimes. This cannot be done analytically for the $v \propto 1/\sqrt{\cos\theta}$ case, but is trivial for the constant speed regime and simple enough for the $v \propto 1/\cos\theta$ case (in the next few lines, for simplicity we use the latitude λ, where $\lambda = \pi/2 - \theta$):

$$v = \frac{v_o}{\sin\lambda} \tag{2.9}$$

where v_o is the velocity at the poles. Rewriting v as the derivative $R\,d\lambda/dt$:

$$R\sin\lambda\,d\lambda = v_o\,dt \tag{2.10}$$

$$\int_0^\lambda R\sin\lambda\,d\lambda = \int_0^t v_o\,dt \tag{2.11}$$

$$1-\cos\lambda = \frac{v_o t}{R} \tag{2.12}$$

In our simulations, we found the latitude as a function of time numerically for the regime of $v \propto 1/\sqrt{\cos\theta}$.

The light-bending effects of gravity were included in this model, using approximate expressions presented in Beloborodov [2002] for the propagation of light emitted from compact objects, such as neutron stars. The overall effect is to increase the surface of the NS visible to a distant observer due to light being bent by the neutron star's gravitational field.

Equation (4) from Beloborodov [2002], rewritten in terms of the redshift z, is an expression describing the contribution to the flux seen by a distant observer from all the surface elements on the neutron (including those which may be "behind" the star):

$$dF = \frac{1}{(1+z)^4} I_o(\alpha) \cos\alpha \frac{dS}{D^2} \tag{2.13}$$

where α is the angle the departing photon direction makes with an axis normal to the surface of the star.

We multiply both sides of equation (2.13) by $4\pi D^2$ and thus get a luminosity on the LHS. We drop the $4\pi(1+z)^{-4}$ expression, since it only scales the total luminosity, and in our models, we allow the overall luminosity scale to vary freely to fit the data. We thus get

$$dL = F \cos\alpha \, dS \tag{2.14}$$

where F is the local flux (in our case this would be the A3 lightcurve from Heger et al. [2007]. Note that the α-dependence of I_o has been removed since in our calculations the local emission only depends on time, not on the emission angle (we assumed isotropic emission).

We want to rewrite this simple expression into one whose variables will be the polar (θ) and azimuthal (ϕ) angles aligned with the rotation axis of a spherical NS. Starting with dS, the surface element on a sphere:

$$dS = d\theta \, d\phi \sin\theta \, R^2 \tag{2.15}$$

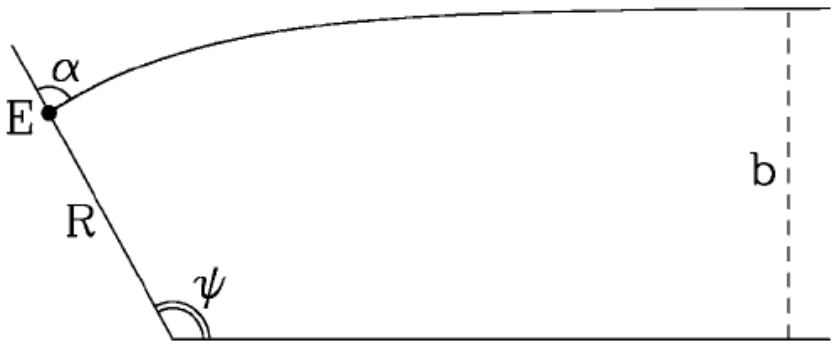

Figure 2–4: A schematic representation of the curved trajectory of a photon being emitted at the NS surface. α is the angle the photon direction makes with an axis normal to the surface of the star. E is the emission point on the surface of the NS, a distance R away from the center, and b is the impact parameter at the observer's location. ψ is the angle formed at the center of the NS by a vector pointing to the observer, and another pointing to E [Beloborodov, 2002].

where R would be the radius of the star, but in our calculations we drop the expression because again it just scales the final luminosity. Next we have $\cos\alpha$. The following expression, relating the angle α to an angle ψ (defined below), is taken from Beloborodov [2002]:

$$1 - \cos\alpha \;=\; \frac{1-\cos\psi}{(1+z)^2} \tag{2.16}$$

The angle ψ in this expression is like the polar angle θ, only it is oriented such that $\psi = 0$ coicides with the observation angle θ_0. To get a visual impression of how the angles α and ψ are related, see Figure 2–4.

To get ψ in terms of θ and ϕ, we write ψ as the inverse cosine of the dot product of an arbitrary coordinate vector and the *observation* vector (i.e. the vector which points to the observer, along θ_0):

$$\cos\psi \;=\; \begin{pmatrix} \sin\theta\,\cos\phi \\ \sin\theta\,\sin\phi \\ \cos\theta \end{pmatrix} \cdot \begin{pmatrix} \sin\theta_0 \\ 0 \\ \cos\theta_0 \end{pmatrix} \;=\; \sin\theta\,\cos\phi\,\sin\theta_0 + \cos\theta\,\cos\theta_0 \tag{2.17}$$

Note that in the second vector, there would be a ϕ_0 to go along with θ_0 in the *observation* vector, but I have set it to 0 for convenience, since the whole star is ϕ-symmetric.

Finally rewriting dL in full yields the expression that is integrated in our calculations to generate lightcurves:

$$dL \;=\; F(\theta,t)\,\left[1-\frac{1-\sin\theta\,\cos\phi\,\sin\theta_0-\cos\theta\,\cos\theta_0}{(1+z)^2}\right]\sin\theta\,d\theta\,d\phi \qquad (2.18)$$

To generate burst spectra time-series, we used all the model features outlined above, only instead of simply taking the local flux and integrating over the star surface, we assumed each patch on the star emitted as a blackbody, with its own temperature, and summed over the star surface, frequency by frequency, to obtain a total burst spectrum. The local flux is as always taken from model A3 presented in Heger et al. [2007], and so a local temperature $T(\theta)$ is obtained from the Stefan-Boltzmann law

$$F \;=\; \sigma T^4(\theta) \qquad (2.19)$$

We then obtain the flux at a particular frequency ν by evaluating

$$F(\nu,T(\theta)) \;=\; \int d\Omega\,\cos\theta\,B(\nu,T(\theta)) \qquad (2.20)$$

where $B(\nu,T(\theta))$ is Planck's law. By integrating this expression

$$F(\nu,T(\theta)) \;=\; \int_0^{2\pi} d\phi\,\int_0^{\frac{\pi}{2}}\sin\theta\,\cos\theta\,B(\nu,T(\theta)) \qquad (2.21)$$

at each time step, summing over many patches of the NS emitting blackbody spectra of different temperatures, we generated a time-dependent spectrum to which we fit a blackbody spectrum and thus obtained the effective temperature for the whole spectrum and an inferred emission area (or normalization).

We did not include any beaming for the emission from the NS surface in our models, as we found that the effects were minimal on the simulation results.

To calculate the constraints on the model parameters, we employed the Bayesian method for evaluating the likelihood of a generated model given a data set to which we did the fitting. More on this can be found in Appendix B.

2.3 *Results: Fitting the lightcurves*

The analysis was performed on an average burst profile generated from ten GS 1826-24 bursts observed during the year 2000 by RXTE (see Figure 2–5 the open squares with error bars, or see figure 1–3, the *middle* set of burst profiles). We performed the simulations for constant spreading speed, as well as the $v \propto 1/\cos\theta$ and $v \propto 1/\sqrt{\cos\theta}$ regimes.

We allowed inclination (or observation angle) parameter i in our model to vary in 5° steps, from 0° (observer is looking down on the pole) to 90° (observer is facing the equator). The spreading time t_s was varied in steps of 0.1 s for the generation of lightcurves, from $t_s = 1$ to $t_s = 13$ seconds. Finally the redshift was varied in steps of 0.02 for the lightcurves and 0.04 for the spectra, in the range $z = 0 - 0.44$.

Since we are mostly interested in the early stages of these lightcurves where spreading would be important, we did statistics on the first $\sim$ 25 seconds of the burst only, which includes the rise and some of the cooling phase. In our simplified model, the effects of spreading, which occurs on a timescale much shorter ($\sim$ 5 s) than the timescale for change in the flux during burst tail ($\sim$ 100 s) would therefore not have an important effect in the latter parts of the burst. Furthermore, the behaviour of the luminosity

in the latter parts of the tail is mostly determined by nuclear physics input. The uncertainties associated with certain reaction rates can create variations in the burst profile, particularly in the tail [Smith et al., 2008]. Thus, to avoid having the shape of the flux lightcurve during the tail influence which of our spreading models would be likeliest, we restricted our analysis to the early portions of the burst.

The best-fit lightcurves for each spreading speed regime are displayed in a plot in Figure 2–5 along with the A3 model burst profile from Heger et al. [2007], the data points and the error bars associated with the latter[3] . Spreading has smoothed the two stage rise in the A3 model from Heger et al. [2007] into good agreement with the average observed burst profile. While the best fit models with v ∼constant and $v \sim 1/\cos\theta$ have a lower reduced chi-square than the best-fit $v \sim 1/\sqrt{\cos\theta}$ model (~ 0.5 compared to ~ 0.8), all three fit the average observed profile very well.

The χ^2_{red} values[4] we find are low, which is suggestive of a very good fit. The fact that the values are below $\chi^2_{red} = 1$ may also be an indication

[3] The uncertainties for this *average* of burst profiles is the standard deviation, at each time bin, between the different lightcurve profiles which make up the average. The error bars do appear to be larger than the scatter in flux from one time bin to the next. This can be attributed to the fact that an individual lightcurve does not show a large scatter from one time bin to the next, thus showing a *smooth* evolution of the flux in time, whereas there is a more substantial scatter in flux at each time bin from one lightcurve to the next. The result, as we see, is a smooth *average* lightcurve with large error bars.

[4] This is the reduced chi squared defined as $\chi^2_{red} = \frac{1}{\nu}\sum_i \frac{(O_i - E_i)^2}{\sigma_i}$. ν is the number of degrees of freedom, defined as $\nu = N - n - 1$, where N is the number of data points, and n the number of fitted parameters in the model. O_i is the observed measurement, E_i is the expected (or modeled) measurement, and σ_i is the error on the observed measurement.

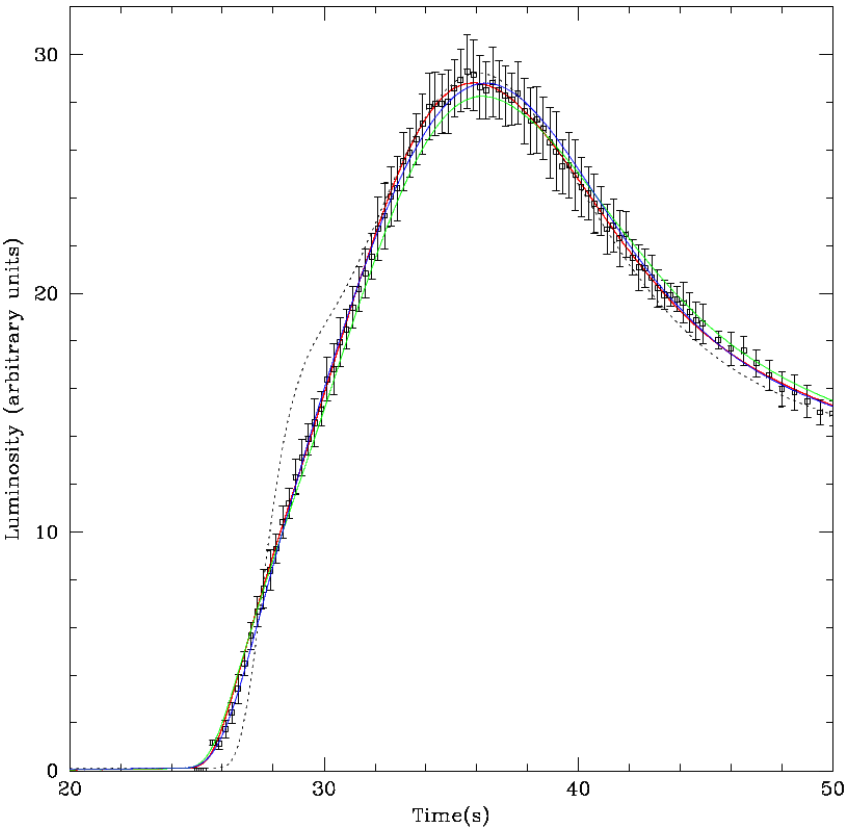

Figure 2–5: A plot of the best fit models for the 3 spreading velocities. v ∼constant is represented by the blue line with parameters $z = 0.2$, $t_s = 6.7$ s and $i = 90°$ ($\chi^2_{red} = 0.539$) , $v \sim 1/\sqrt{\cos\theta}$ in green with parameters $z = 0.12$, $t_s = 9.5$ s and $i = 50°$ ($\chi^2_{red} = 0.792$) and $v \sim 1/\cos\theta$ in red with parameters $z = 0.1$, $t_s = 8.5$ s and $i = 20°$ ($\chi^2_{red} = 0.455$). The dotted line represents model A3 from Heger et al. [2007], and the open squares with error bars represent an average burst profile observed with RXTE in 2000 (see Galloway et al. [2004]).

that the uncertainties over-estimated. According to the χ^2 distribution, the probability that a random set of ν data points from the parent distribution would yield a $\chi^2_{red} \leq 0.5$ is $\leq 0.002\%$ (84 degrees of freedom).

The best fit z parameters are in the 0.1 to 0.2 range, implying a NS with a low mass and large radius, such as, for example a star with physical parameters $M = 1.2M_\odot$ and $R = 15$ km, which would have a redshift of $z = 0.15$. This is suggestive of a stiff equation of state. The lower limit of that range, $z = 0.1$, is a bit unrealistic, as there are not many equations of state which encompass NSs with such a low redshift (see for e.g. Lattimer

and Prakash [2001]) at reasonable masses ($\gtrsim 1.0 M_{\odot}$; see Thorsett and Chakrabarty [1999] for measurements of NS masses in binaries. See also Woosley et al. [2002] for NS mass restrictions from formation).

The inferred spreading time t_s from our best fit models are higher than what one might guess from looking at the rise time of the burst profile, which is approximately 5 s. In our simulations, the peak flux is often reached before the whole star surface becomes ignited. While the increase in the emitting area, which occurs relatively slowly in our models ($7 - 10$ s), is an important contributor to the overall flux, the strength of the flux in the regions that are *facing* the observer, which has a ~ 5 s rise timescale, has a more important influence on how rapidly the overall luminosity will reach its peak.

To get an understanding for the constraints on the model parameters from comparisons with the average observed burst profile, we computed the model probabilities for the whole evaluated parameter space (see Appendix B). Figures 2–6, 2–7 and 2–8 show plots of the 68%, 95% and 99.7% confidence interval contours.

We note strong correlations between z & t_s in all three contour plots. This can be understood by being aware that the effect of the redshift in our models is two-fold: firstly it enhances the visible region of the NS surface, and secondly it dilates in time any signal coming from surface. To illustrate this point, let $t_{s,true}$ be the "true" spreading time as described by our model and z_{true} the "true" redshift. The *apparent* spreading time we would measure on Earth (or at almost any other location far away from the source), considering only the time-dilation effect of z, would be

$$t_{s,Earth} = t_{s,true}(1 + z_{true}) \tag{2.22}$$

Therefore, when trying to find the best t_s and z given the apparent spreading time $t_{s,Earth}$ there will naturally be some leeway for those two parameters to move in opposite directions. However, the degeneracy does appear to be limited to finite regions of the t_s-z contour plots, beyond which the degeneracy breaks down. This can be attributed to the *first* effect of the redshift outlined above, which cannot be "imitated" by changing t_s.

The common result to all the spreading regime models is that a combination of low redshift ($\lesssim 0.2$) and long spreading time ($\gtrsim 7$s) is needed in the models to fit the early parts of the burst. Models with a combination of a shorter spreading time with larger redshift do not fit the rise well as the two-stage rise present in the local flux does not get sufficiently smeared out in models with short spreading times.

The t_s-z correlations in all three spreading speeds show an interesting characteristic. While the degeneracy present in the three t_s-z plots (shown in Figures 2–6, 2–7 and 2–8) prevents us from determining with any certainty the actual values of t_s and z, the fact that the confidence intervals draw out what appears to be a slope common to all three speed regimes implies a common $t_{s,Earth}$ (see Equation 2.22) for all three models. Taking the best fit t_s and z parameters for each speed regime, we find $t_{s,Earth}$ values of 8.05, 9.35, and 10.60 seconds for the spreading velocity regimes $v \sim$ constant, $v \sim 1/\cos\theta$ and $v \sim 1/\sqrt{\cos\theta}$, respectively. The proximity of these values implies that, for example, if we knew from a separate measurement the value of z, our models would all imply a similar t_s, to within $\sim 20\%$.

The inclinations do not appear to be very well constrained in our contour plots, particularly for $v \sim 1/\sqrt{\cos\theta}$. There is in fact a feature which is clearly apparent in the i-z plot of figure 2–8 but which holds true for all

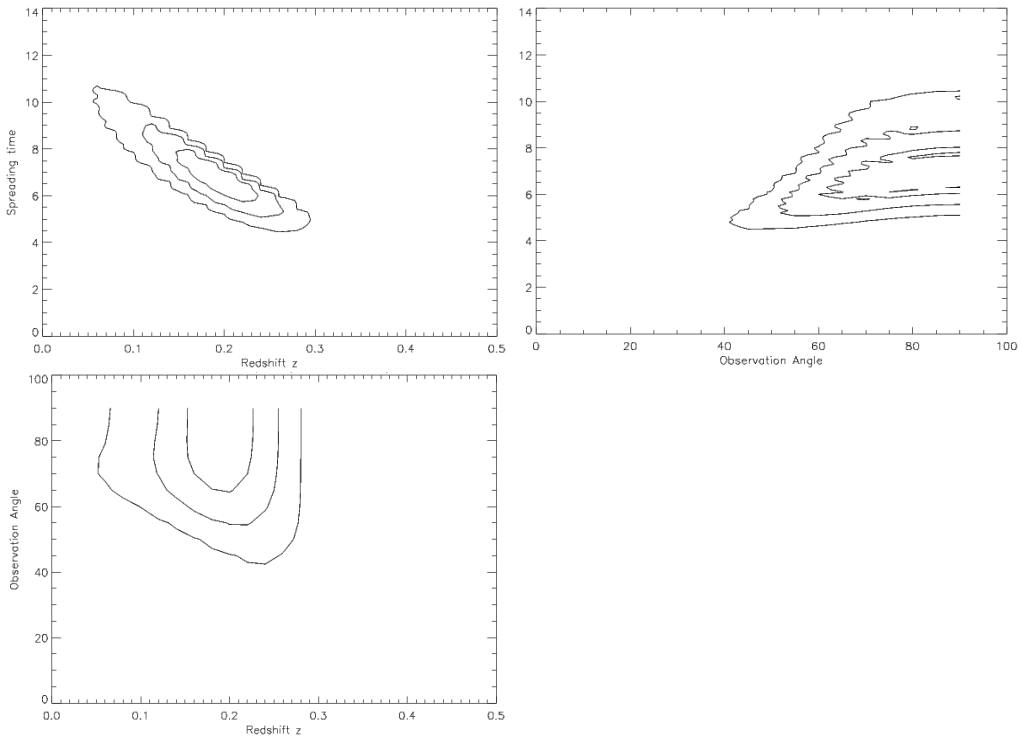

Figure 2–6: The contour plots of the probabilities for the constant spreading speed models with respect to their varying parameters. The contour lines are spaced at $99.7\%, 95\%$ and 68% confidence intervals

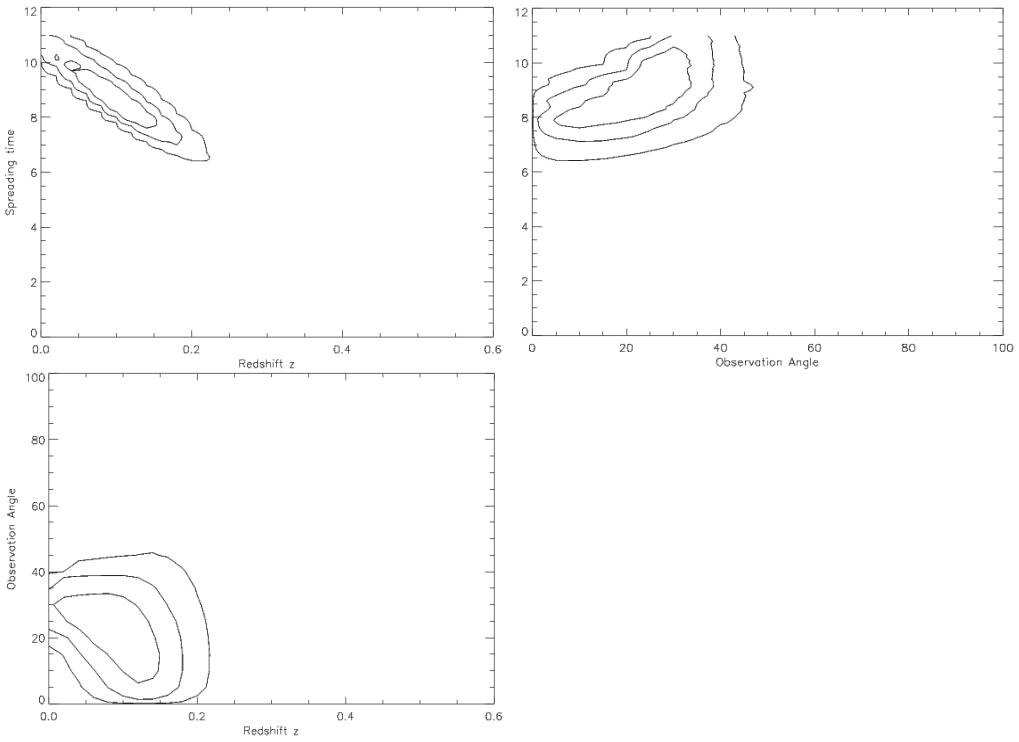

Figure 2–7: The contour plots of the probabilities for the $v \sim 1/\cos\theta$ models with respect to their varying parameters. The contour lines are spaced at 99.7%, 95% and 68% confidence intervals

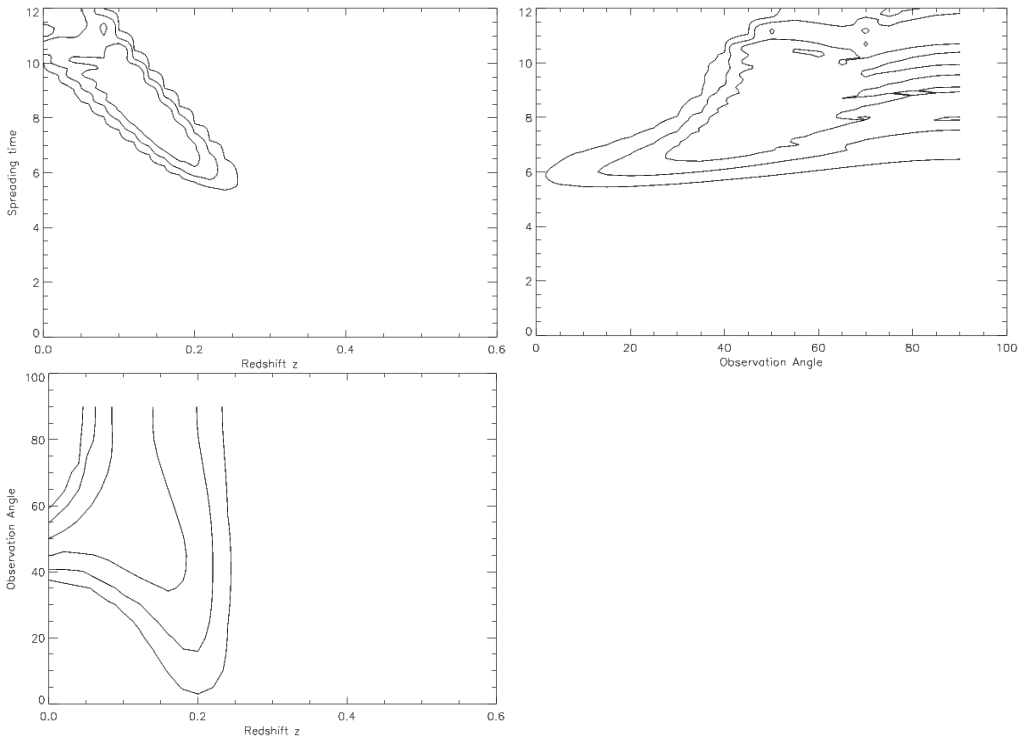

Figure 2–8: The contour plots of the probabilities for the $v \sim 1/\sqrt{\cos\theta}$ models with respect to their varying parameters. The contour lines are spaced at 99.7%, 95% and 68% confidence intervals

the spreading speed models, and that is that as you move up in redshift, the inclination becomes less and less constrained. Since increasing the redshift makes more of the NS surface visible to the oberver (for example when $z = 0.22$, $\sim$75% of the surface is visible to a distant observer), the difference between observation angles becomes less important.

The $v \sim$ constant model suggests a high inclination, with the best fit model having $i = 90°$. This is contrary to the results of Homer et al. [1998] who find that from the small amplitude of the optical modulations associated with the binary orbit in this source, the system must have a low inclination ($\lesssim 70°$). The 68% confidence interval in Figure 2–6 does however extend to inclinations lower than 70°, so good fitting models with $i \lesssim 70°$ do exist.

Overall, these results do not allow us to meaningfully discriminate between the spreading speed regimes.

2.4 *Results: Fitting the blackbody radius*

This analysis was performed on the same 10 observed bursts from the previous section, this time looking at the spectroscopic data, namely the evolution of the inferred blackbody area ($(R/d)^2$, where d is the distance set to 10 kpc, and radius is the inferred radius of a spherical blackbody). As described in §2.2, we generated time-dependent model burst spectra from which we extracted a theoretical blackbody area evolution, dependent on the model parameters, which we then fitted to the average observed profile.

To generate the chi-squared grid in our parameter space, we took the χ^2 sum of our models with a single, averaged blackbody radius profile. We computed the average profile by taking an average of the 10 blackbody area profiles. To compute the uncertainties, we evaluated the 1σ scatter

(divided by $\sqrt{N}$, where N is the number of measurements; $N = 10$ in this case) at each time step over the 10 profiles (similarly to the way the errors were computed for the lightcurves, in the previous section), since we found that the scatter at each time step between the different profiles was about a factor of 2 larger than errors in the individual profiles.

For these simulations, we utilized the same values for the inclination parameter i as in the previous section. The spreading time t_s was varied this time in larger steps of 0.5 s, again from $t_s = 1$ to $t_s = 13$ seconds. Finally, for the redshift, we used both the same range as we used in fitting the lightcurves, that is $z = 0 - 0.44$, as well as the more plausible range of $z = 0.16 - 0.44$ for comparison, in steps of 0.04.

Figure 2–9 shows the best-fit models for each of 3 spreading speed regimes with the redshift parameter range of $z = 0 - 0.44$. What we find is that for all three spreading speed models, the preferred redshift is around $z = 0$, an unrealistic redshift for a NS surface. Nonetheless, the best-fit simulations for all three speed regime agree very well with the average observed profile, which is linear in shape.

Figure 2–10 shows a plot similar to 2–9 with the redshift range now restricted to $z = 0.16 - 0.44$. What we find is that while the χ^2 for the best-fit model with v ∼constant remains small, and almost unchanged in this smaller range, for $v \sim 1/\cos\theta$ and $v \sim 1/\sqrt{\cos\theta}$ the values of χ^2_{red} increase to values of 3.4 and 2.2, suggestive of fits which are unacceptable (see captions in figures 2–10 and 2–9 for all the reduced chi-squared values). Again referring to the χ^2 distribution, we find that the probabilities associated with obtaining $\chi^2_{red} \geq 3.4$ and $\chi^2_{red} \geq 2.2$ (with 55 degrees of freedom) are both $< 10^{-6}$.

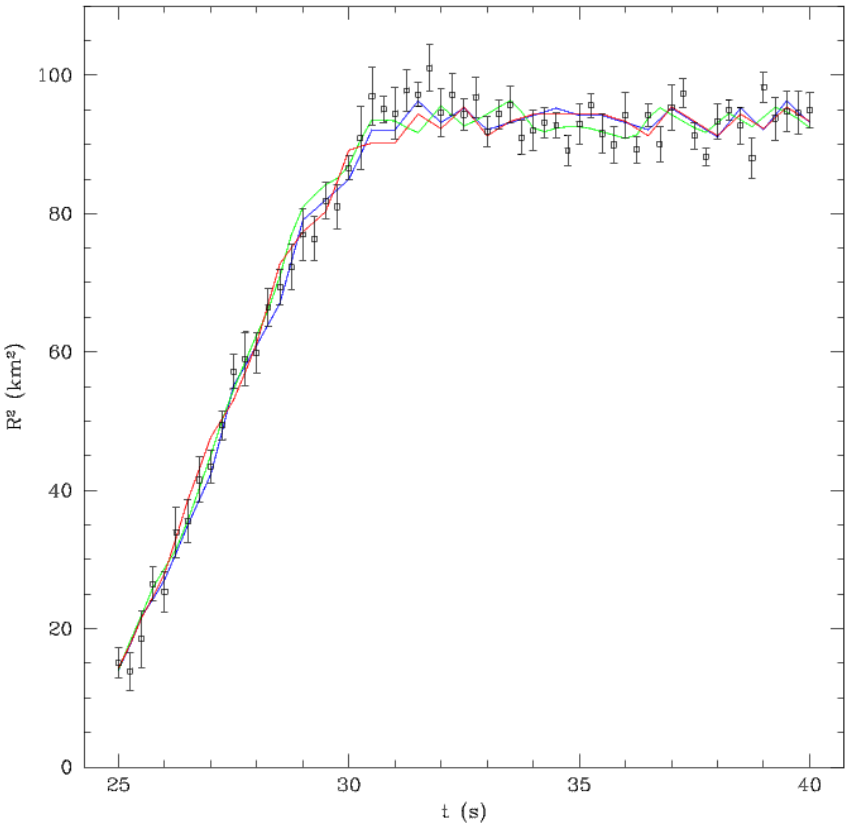

Figure 2–9: A plot of the best fit models for the 3 spreading velocities, with the redshift range of $z = 0 - 0.44$. $v \sim$constant is represented by the blue line with parameters $z = 0$, $t_s = 8$ s and $i = 5°$ ($\chi^2_{red} = 1.30$), $v \sim 1/\sqrt{\cos\theta}$ in green with parameters $z = 0.04$, $t_s = 6.0$ s and $i = 15°$ ($\chi^2_{red} = 1.34$) and $v \sim 1/\cos\theta$ in red with parameters $z = 0$, $t_s = 6.5$ s and $i = 10°$ ($\chi^2_{red} = 1.62$).

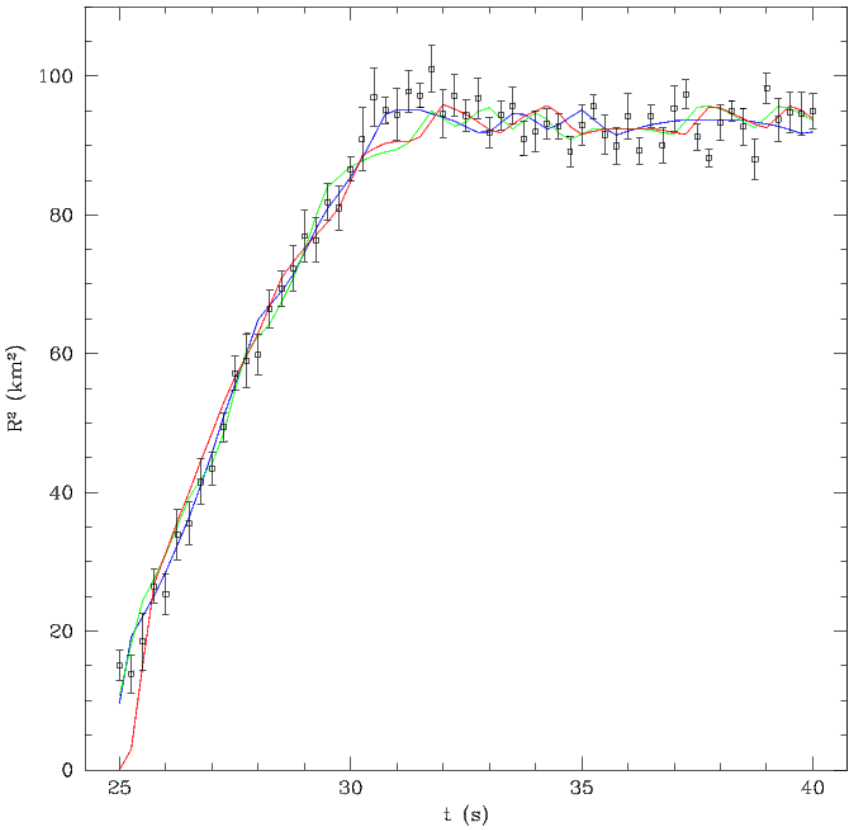

Figure 2–10: A plot of the best fit models for the 3 spreading velocities, with the redshift range of $z = 0.16 - 0.44$. $v \sim$constant is represented by the blue line with parameters $z = 0.4$, $t_s = 4.0$ s and $i = 15°$ ($\chi^2_{red} = 1.47$), $v \sim 1/\sqrt{\cos\theta}$ in green with parameters $z = 0.16$, $t_s = 5.0$ s and $i = 15°$ ($\chi^2_{red} = 2.19$) and $v \sim 1/\cos\theta$ in red with parameters $z = 0.16$, $t_s = 5.5$ s and $i = 5°$ ($\chi^2_{red} = 3.39$).

For latitude-dependent spreading, the front slows down as it approaches the poles, and this is conducive to an emitting area whose slope turns over (with a negative second derivative with respect to time). This is why the latitude-dependent spreading speed models prefer a very low inclination $i < 15°$. For an observer looking down at the pole, the net area increase (a projection of the actual area, that is $dS_{proj} = dA_{real} \cos\theta$, where θ is the polar angle) will appear to be closer to linear. Increasing the redshift, thereby revealing more of the NS surface to the observer, washes out this projection effect, giving blackbody area evolution curves whose slopes turn over.

From the comparison of fits between simulations done with the longer and shorter ranges for z, it appears $v \sim$constant models are better able to fit the data for a wider range of parameters, owing to the linear shape of the average observed blackbody area curve.

2.5 *Discussion*

We have shown that the discrepancy with observations present in the burst rise of model A3 from Heger et al. [2007] can be resolved if that model is incorporated as the local flux in a simple spreading model. While the comparisons of our models to the observed lightcurves and blackbody emission areas has not allowed us to discriminate meaningfully between burning front speed regimes, the good agreements suggest that spreading is at least provides a possible explanation for the shape of the emission area evolution.

It should be mentioned that the good overall agreement with the observed lightcurve is not surprising, as the local flux we used already had fairly good agreement with the data, barring the rise. Our spreading models

had the effect of washing out the two-stage rise present in the A3 model, and manipulating the overall shape to almost exactly match the early part of the lightcurve.

It can be argued that for the blackbody area fitting, the spreading model was more essential. How the burst spectrum during the rise, with its slow and linear increase in inferred emission area, could be reproduced without a spreading model is not immediately clear (see Chapter 3 for more on this).

In the fitting of the blackbody area profiles, we mentioned that we took the uncertainty for the average profile to be the spread between the measured values of the individual profiles. We also mentioned the reason for this: the spread was approximately a factor of two larger than the individual errors. The same procedure was used to determine the uncertainties in the lightcurve profiles. This may be an indication that the individual profiles from burst to burst are different, and that they do not reflect an indentical underlying set of characteristics. As such, it could be more informative, in future work, to fit to individual burst emission profiles, both for the lightcurves and emission area.

The best fitting model parameters from the two sections (§2.3 and §2.4) have only limited agreement. By placing the best fit parameters for the blackbody area fits into the corresponding parameter space of figures 2–6, 2–7 and 2–8, we find that none of the best-fit parameters for blackbody area simulations fall within the 68% confidence intervals of the best-fit lightcurve simulations. The only two best-fit models which fall within the 99.7% interval are the $v \sim 1/\cos\theta$ and $v \sim 1/\sqrt{\cos\theta}$ regime models with the redshift range of $z = 0 - 0.44$. This does not however imply that there are no sets of parameters which fit both the lightcurves and emission area

profiles simultaneously. Indeed without the probability constraints on the emission area fits, all we can assert is that the *best-fit* emission area models do not fall within the 68% confidence interval about the best fit parameters for the lightcurve fits. In future work, it may be informative to find the constraints on the blakbody area fits with probability plots, and furthermore to try to fit the lightcurve and emission area profiles simultaneously for a set of parameters, to see whether we could obtain more restrictive constraints on our parameters, as well as the spreading speed regimes.

CHAPTER 3
The spectral evolution of burst emission from GS 1826-24

3.1 *Introduction*

There have been ongoing attempts to characterize and understand the emission spectrum in GS 1826-24. Wide band measurements of its persistent emission (emission between bursts) include results from observations done with *Ginga* and *OSSE* by Strickman et al. [1996], *BeppoSAX* [in 't Zand et al., 1999], *RXTE* [Barret et al., 2000], *Chandra* and *RXTE* simultaneously [Thompson et al., 2005] and *INTEGRAL* [Cocchi et al., 2010]. While the observations took place at different times, these studies have consistently found that this source has emission at and above 100 keV, and that a cut-off power-law with photon index around $\Gamma \sim 1.7$ and a cutoff of around $\sim$ 50keV yields good fits to the high-energy data [del Sordo et al., 1999] [Strickman et al., 1996] [Barret et al., 2000]. The common interpretation for the origin of this high-energy tail is Comptonization of soft seed photons by a hot electron plasma, and such models have been used to find good fits to the observed high-energy spectra [Thompson et al., 2005] [Cocchi et al., 2010]. Typical electron temperatures inferred are in the $15 - 20$ keV range but Thompson et al. [2005] found that an additional $6 - 8$ keV Compton component was necessary.

During an X-ray burst, the flux increases by 1 or 2 orders of magnitude and the emission becomes dominated by what is believed to be the hot NS surface. The burst emission is usually well fit by a blackbody spectrum with peak temperatures of around 2-3 keV (e.g. Galloway et al. [2008]). There is

however evidence for the burst spectrum having significant deviations from that of a blackbody.

Firstly the fitted temperatures during bursts are often found to exceed the Eddington *temperature* limit of [Lewin et al., 1993]

$$kT_{Edd,\infty} = 2.28\,\mathrm{keV}\left(\frac{M}{1.4M_{\odot}}\right)^{1/4}\left(\frac{R}{10\mathrm{km}}\right)^{-1/2}(1+z)^{-3/4}\,(1+X)^{-1/4} \quad (3.1)$$

(where M is the NS mass, R the NS radius, z the gravitational redshift and X the hydrogen mass fraction of the accreted gas) for a blackbody emitter, without the expected evidence for photospheric radius expansion (PRE).

The modeling of NS atmospheres has shown that NS surface emission may have a blackbody-like shape, but with a fitted temperature (also called *colour* temperature) higher than the *effective* temperature an equivalent blackbody would have with the same flux (see London et al. [1984], London et al. [1986], Madej et al. [2004], Majczyna et al. [2005]). The ratio of colour to effective temperature T_c/T_{eff} in these models is typically in the 1.2 to 1.8 range, depending on the surface gravity, surface flux, and atmosphere composition. This effect is attributed to the strong energy dependence of the free-free opacity and the presence of electron scattering in the atmosphere. These models have traditionally been used to explain how bursts which despite appearing to reach super-Eddington temperatures may have sub-Eddington fluxes[1] .

[1] recently Boutloukos et al. [2010] disputed this, claiming that conventional atmospheric models "do not provide a statistically acceptable description of the high-precision [...] burst spectra obtained using RXTE", deducing that many bursts with super-Eddington colour temperatures are genuinely super-Eddington in flux as well, and suggested that the NS's magnetic field confines the atmosphere, preventing PRE.

Furthermore, time-resolved spectroscopy of bursts from several sources including GS 1826-24 shows a sudden decrease in the inferred emission area in the burst tail (see in't Zand et al. [2009] for GS 1826-24 in particular, and see Galloway et al. [2008] for many other sources). Given that the burst spectrum is well fitted by a blackbody, it is expected that the during the burst tail the inferred emission area should stay constant with the temperature diminishing with the flux, as $T \propto F^{1/4}$ (according to the Stefan-Boltzmann law). What is in fact observed, particularly in bursts from GS 1826-24 is that the fitted blackbody radius suddenly starts shrinking after about 100 seconds, eventually settling to a value of around one third of the peak radius at roughly $t = 200$ s. As was mentioned before, attempting to understand this aspect of the burst will be the topic of this chapter.

Lastly, it is important to mention that while burst spectra are often well described by a blackbody spectrum, it is not always the case. Nakamura et al. [1989] found that bursts from the source 4U 1608-52 (which they referred to as X 1608-52 in their article) which occured during periods when the persistent luminosity was low ($< 1 \times 10^{37}\,\mathrm{erg\,s^{-1}}$) had spectra with high-energy tails, and overall could not be acceptably fit by a blackbody. Interpreting this as Comptonization of a blackbody spectrum, they employed the (optically thin) Comptonized blackbody model of Nishimura et al. [1986] and found good fits (with plasma temperatures of $kT_e \approx 100$ keV) for those bursts which could not be acceptably fit by a blackbody.

3.2 *Spectral behaviour in the tails of bursts from GS 1826-24*

As was mentioned in the previous section, time-resolved spectroscopy of X-ray bursts from GS 1826-24 shows an inferred emission area which suddenly decreases after ~ 100 seconds (see 1.4)

To try to understand the observed behaviour of the spectrum, we made a simple model of the NS emission; by assuming that the NS surface is emitting like a blackbody and once again using the flux from model 'A3' presented in Heger et al. [2007] as the surface emission.

3.3 *Subtracting a blackbody*

Initially, we looked at the possibility that the behaviour described above was due to the subtraction of a pre-burst component of the spectrum which might no longer be present in the burst spectrum. van Paradijs and Lewin [1986] suggested that if a NS in an X-ray burst source is sufficiently hot to give a significant blackbody contribution to the persistent emission, the *blackbody radii* inferred from the analysis of the burst spectra, which normally involves subtracting the persistent emission from the burst emission, would contain systematic errors, particularly when the burst flux is at its lowest. Subtracting a Planck spectrum (the fixed pre-burst photospheric emission) from another Planck spectrum (the variable burst emission) yields a spectrum which is non-Planckian. For a small difference in temperature (ΔT) between the two Planck spectra, they showed that the flux is written as

$$F_\nu = F_{burst} - F_{pre\text{-}burst}$$

$$F_\nu = B_\nu(T_0 + \Delta T) - B_\nu(T_0)$$

$$F_\nu \approx \frac{dB_\nu}{dT}\Big|_{T_0} \Delta T$$

From the last expression, it can be seen that for small ΔT, the spectrum would be that of the derivative of the Planck spectrum. If a blackbody were fitted to this spectrum from which a temperature and area were extracted, one would find that as ΔT gets smaller, the fitted temperature would remain roughly constant (but at a value 35% greater than T_0 van

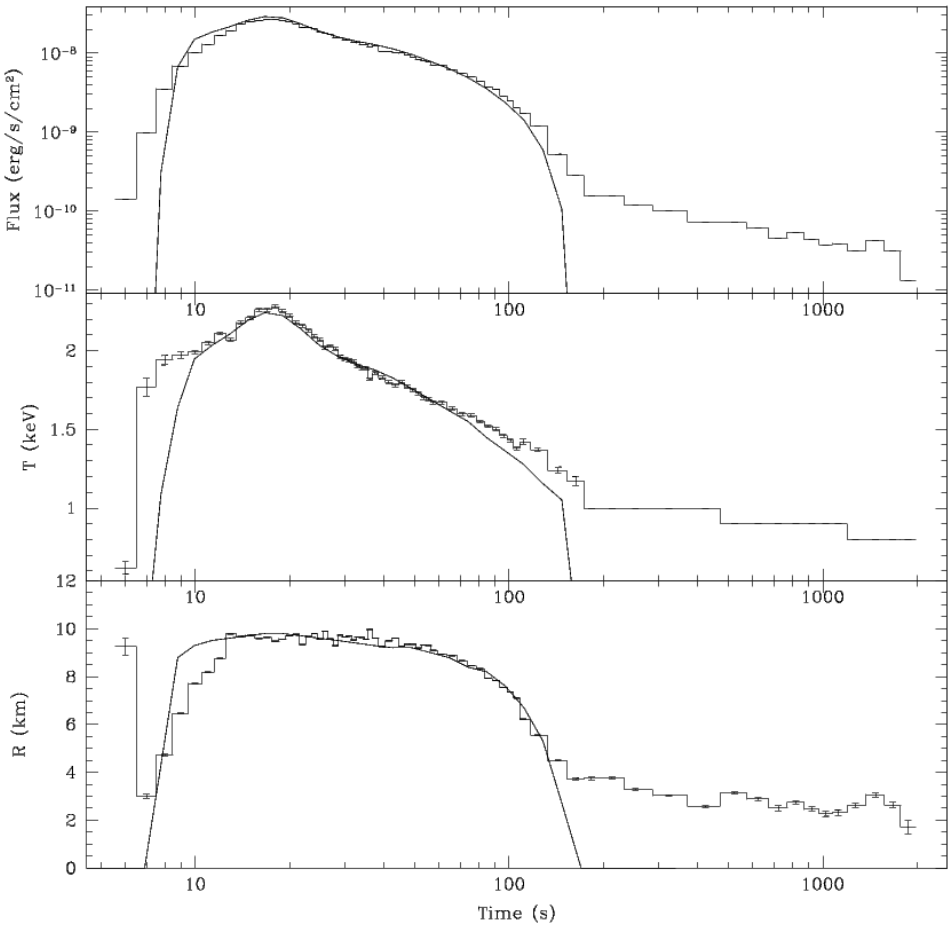

Figure 3–1: A comparison between the flux, temperature and radius profiles from burst observations (histogram) and the best fit we could find for those profiles by "subtracting a blackbody" (solid curve). The parameters we used are: $f_c = 1.25$, a distance of 6.07 kpc, a neutron star radius of 10 km, and subtracted blackbody with the same normalization, and with temperature $kT = 0.75$ keV. Best fit for the 'subtraction' method.

Paradijs and Lewin [1986]) while the normalization would get progressively smaller. This suggests that the subtraction of a fixed blackbody spectrum from a Planck spectrum whose temperature is diminishing with time may give the correct behaviour for the fitted 'blackbody radius'.

3.4 *Comptonization by a cloud of electrons*

We also tried to model the effects of the NS burst emission being Comptonized by a cloud of electrons. We based our calculations on the

Kompaneets equation, an advection-diffusion equation describing the evolution of a spectrum undergoing repeated Compton scattering by non-relativistic electrons. The equation is [Rybicki and Lightman, 1979]

$$\frac{\partial n}{\partial y} = \frac{1}{x^2}\frac{\partial}{\partial x}\left[x^4\left(\frac{\partial n}{\partial x} + n + n^2\right)\right] \tag{3.2}$$

where $y = (kT_e/m_ec^2)\tau$ is the Compton parameter, n the photon phase space density in momentum-position space and $x = h\nu/kT_e$, the reduced photon energy. The Compton parameter y is a measure of how much a photon will change its energy as it traverses a medium. The first term in the parenthesis $\partial n/\partial x$ is the term for diffusion in energy space, while the second is the advection of the distribution n. The n^2 term accounts for the fact that photons tend to mutual occupation of the same quantum state.

In the derivation of the Kompaneets equation, it is assumed that $h\nu \ll kT_e \ll m_ec^2$. That is, that the photon energy is much less than that of the electrons and that the electrons are non-relativistic. In finding a model which best reproduced the photometric data, we needed to explore electron temperatures comparable to, as well as higher and lower than, the photon energy. In deriving the Kompaneets equation, one has to find the value of Δ, the shift in photon frequency per scattering in terms of the initial and final photon and electron energies and momenta. In the nonrelativistic limit ($h\nu$, $kT_e \ll m_ec^2$), it is given by

$$h\Delta = -\frac{h\nu c}{m_ec^2}\boldsymbol{p}\cdot(\boldsymbol{n} - \boldsymbol{n'}) - \frac{(h\nu)^2}{m_ec^2}(1 - \boldsymbol{n}\cdot\boldsymbol{n'}) \tag{3.3}$$

where $\boldsymbol{p}$ is the initial electron momentum and $\boldsymbol{n}$, $\boldsymbol{n'}$ are the initial and final photon directions, respectively. If we estimate the momentum of the thermal population of electrons as $\boldsymbol{p} \sim m_ev \sim m_e\sqrt{kT_e/m_e}$, then the ratio of the

second term to the first term in equation 3.3 is

$$\sim \sqrt{\left(\frac{h\nu}{m_e c^2}\right)\left(\frac{h\nu}{kT_e}\right)} \tag{3.4}$$

If $h\nu$ is large enough, then this term cannot be neglected as is done in the derivation of the Kompaneets equation (see equation (7.53) in Rybicki and Lightman [1979]). With this extra term in the expression for Δ, the *modified* Kompaneets equation is then [Chen and You, 1993]

$$\frac{\partial n}{\partial y} = \frac{1}{x^2}\frac{\partial}{\partial x}\left[x^4\left(1+\frac{7}{10}\frac{kT_e}{m_e c^2}x^2\right)\left(\frac{\partial n}{\partial x}+n+n^2\right)\right] \tag{3.5}$$

In our calculations, we dropped the n^2 term since we found that it is much smaller than the other two. We also chose for practical reasons to deal explicitly with the energy flux instead of n, the photon phase space density. As such, we rewrote the modified Kompaneets equation in terms of E, the photon energy density, using the fact that $E \propto x^3 n$ and that dropping the n^2 term renders the equation linear:

$$\frac{\partial E}{\partial y} = x\frac{\partial}{\partial x}\left[\left(1+\frac{7}{10}\frac{kT_e}{m_e c^2}x^2\right)\left(x\frac{\partial E}{\partial x}+E(x-3)\right)\right] \tag{3.6}$$

Lastly, for practical purposes related to the integration of this equation, we rewrote it with logarithmic spacing in energy, in terms of z, where $x = 10^z$. The equation thus takes on this form:

$$\frac{\partial E}{\partial y} = \frac{1}{\ln 10}\frac{\partial}{\partial x}\left[\left(1+\frac{7}{10}\frac{kT_e}{m_e c^2}10^{2z}\right)\left(\frac{1}{\ln 10}\frac{\partial E}{\partial x}+E(10^z-3)\right)\right] \tag{3.7}$$

We integrated this equation numerically using the implicit scheme for the Fokker-Planck equation (of which the Kompaneets and modified Kompaneets equations are special cases) from Chang and Cooper [1970]. The boundary conditions were set at the lower and upper bounds in frequency x such that the number of photons per unit volume ($\int nx^2\,dx =$

$\ln 10 \int E\, dz$) is a constant. Specifically, we ensured that the expression inside the last set of brackets from equation 3.7 vanished at the boundaries.

Let $z = z_0, z_1, ..., z_j, ..., z_{J-1}, z_J$ be the equally spaced integration grid points. The condition for vanishing flux at the energy boundaries

$$\frac{1}{\ln 10}\frac{\partial E}{\partial x} + E(10^z - 3) = 0 \tag{3.8}$$

can be rewritten in a finite differencing scheme in terms of the z grid points as

$$\frac{1}{\ln 10}\frac{E_{j+1} - E_j}{\Delta z} + E_j(10^{z_j} - 3) = 0 \tag{3.9}$$

where Δz is the spacing between any two consecutive grid points ($\Delta z = z_{j+1} - z_j$). Setting $j = 0$ and $j = J - 1$ in this expression yields the boundary conditions to be set at the lower and upper end of the z grid, respectively, when performing the integration.

3.5 *Results*

Keeping the NS radius fixed at the canonical value of 10km, the distance fixed at $d = 6.07$kpc [Heger et al., 2007], and the colour correction $T_c/T_{\rm eff}$ close to a value of 1.35 (typical value from models presented in Madej et al. [2004] or London et al. [1986]), we tried to find by varying the electron temperature T_e and the Compton y parameter the model which best reproduced the data. By eye, we found that setting $y = 0.1$, $T_e = 2.2$keV and $T_c/T_{\rm eff} = 1.27$ yielded a good fit (see Figure 3–2). The fitting was done in the photon energy range of 4-20 keV, the same energy range analyzed from RXTE's PCA in in't Zand et al. [2009] to generate the spectroscopic data against which we compared our models. While the surface flux we used in the model was already a very good fit to the luminosity data (see Heger et al. [2007] and in't Zand et al. [2009]), it had

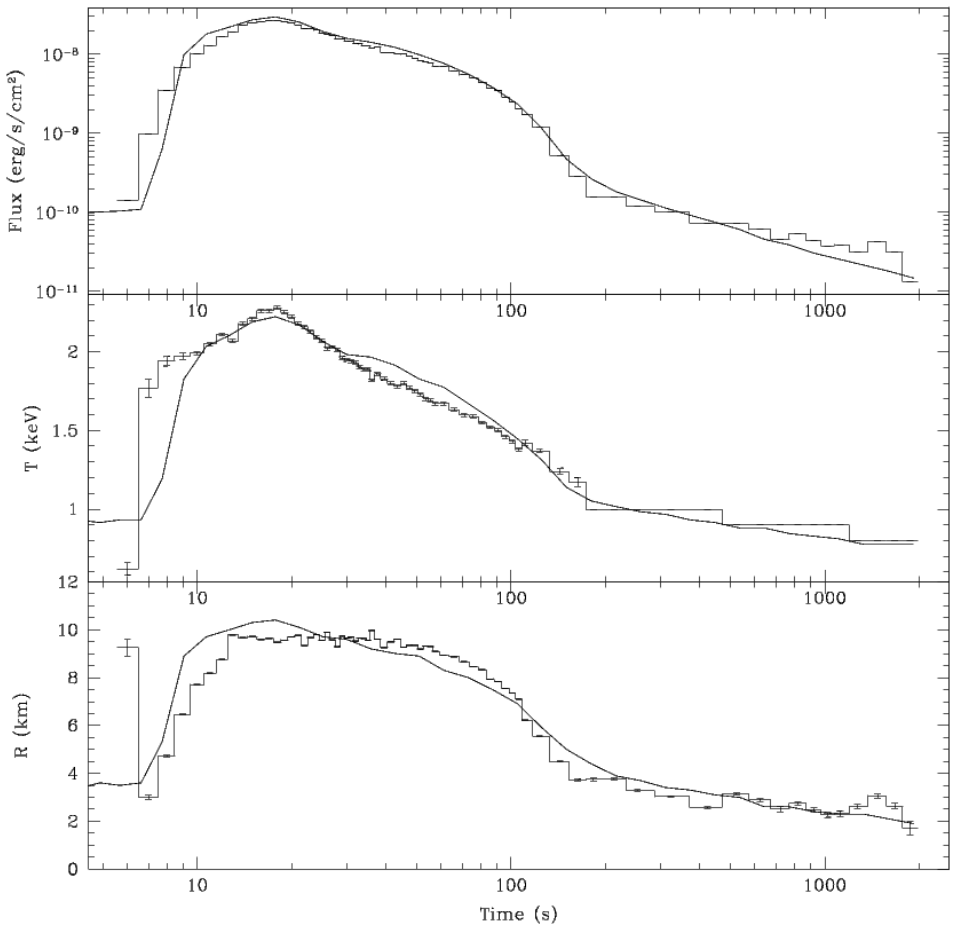

Figure 3–2: A comparison between the flux, temperature and radius profiles from burst observations (histogram) and from Comptonizing a blackbody (solid curve). The parameters we used are: $f_c = 1.27$, a distance of 6.07 kpc, a neutron star radius of 10 km, a Compton paramter of $y = 0.1$, and an electron temperature of $T_e = 2.2$ keV.

to be recomputed after Comptonization since the scattering changes the overall energy of a photon spectrum. The best-fit Comptonization model we found doesn't affect the overall energy of the spectrum very much since the y parameter in this model is small.

The comptonization of a blackbody spectrum using the modified Kompaneets equation in the low y regime has the effect of softening the slope of the Wien tail, thus hardening the spectrum. By fitting a Planck spectrum to this, one finds a higher temperature. In the low y regime, the overall luminosity doesn't change very much (as can be noted by looking at

Equation 3.6), and so an increase in the temperature implies a decrease in the blackbody radius since

$$L = 4\pi R^2 \sigma T^4 \tag{3.10}$$

We found that this effect is more pronounced when we only fit the narrow $4 - 20$ keV interval of the spectrum (more on this in the discussion).

3.6 *Discussion*

We've shown that by using a simple model where a blackbody spectrum is Comptonized by a cloud of electrons, we were able to adequately reproduce the behaviour seen in the latter part of the bursts. We've also shown that while we were able to reproduce the effect described in van Paradijs and Lewin [1986] of a diminishing blackbody area caused by the subtraction of one blackbody from another (see §3.3), it was impossible to attribute the late behaviour of the burst spectrum solely to that effect. It should be noted that for this source, the latter result was partly expected given the results of Cocchi et al. [2010] based on the wide-band observations of the persistent emission from GS 1826-24 done with *INTEGRAL* in 2003 and 2006. They found that, unlike the results of earlier observations reported in in 't Zand et al. [1999], they could not detect a soft (in the ~ 1 keV range) blackbody component in the persistent spectrum. They found the 90% confidence upper limits for a 1 keV blackbody component detection at a distance of 7 kpc to be $R < 1.0$ km and $R < 0.7$ km for the 2003 and 2006 sets, respectively. From the simulations done similar to the one presented in §3.3, we can assert that these upper limits are too low to reproduce the effect described in van Paradijs and Lewin [1986]. The burst observations against which we compared our models were gathered with *RXTE* and *XMM-Newton* from the middle of the year 2000 to early 2007, a time during which Cocchi et al.

[2010] gathered their data with *INTEGRAL*. This implies that there would not have been a notable blackbody component subtracted from the burst emission.

Decreases in the inferred blackbody radius are usually attributed to colour corrections associated with non-Planckian surface spectra emission, since $R_{bb} = R_\infty f_c^{-2}$ [Suleimanov et al., 2010], where R_{bb} is the blackbody radius, and R_∞ the apparent stellar radius. Colour correction changes with surface flux (e.g. [Madej et al., 2004]), and thus could plausibly explain a decreasing blackbody radius during the tail, where the surface flux is continuously diminishing. The required colour correction factor required to account for a drop in the blackbody radius by a factor of 5 as is observed is ≈ 2.24. The maximal colour correction factors found in atmospheric models are $\lesssim 1.9$ (e.g. Madej et al. [2004], London et al. [1984]).

Our comptonizing model does introduce its own colour correction by shifting the temperature upwards which shifts the radius down (to conserve total luminosity). However, this alone is not sufficient to account for the $\sim 70\%$ decrease in blackbody radius that our model produces. Restricting our fitting to the $4 - 20$ keV window also plays an important role. By only "seeing" the high-energy partion of the spectrum, including the tail that comptonization produces, the fitting routine yields blackbody spectra with higher temperatures than if the fitting was being done over the whole spectrum.

A point which is relevant to the previous chapter is that an effect similar to the dimishing radius occurs in reverse time during the burst onset, as can be noted by looking at figure 3–2 for early times. The rise doesn't quite align with the data points; the observed radius evolution appears more linear and the "rise" appears to be slower. However, there is a clear

upward slope in the theoretical curve, mimicking the effect of spreading. In this Comptonization model, there is no spreading; the emission is from the whole star simultaneously. Perhaps we could tweak our model so that the early parts of the blackbody radius evolution could be made to better agree. Regardless of that, the point we wish to make is that an increasing *inferred* emission area cannot be solely attributed to burst spreading, i.e., an *actual* increasing emission area.

Although we modeled the Comptonization as a process that would occur after the photons had been emitted from the NS atmosphere, the good agreement of the $kT_e = 2.2$ keV plasma model could reflect the temperature of a plasma that is near, or a part of, the NS atmosphere, since the latter can easily reach that temperature during an X-ray burst.

In future work, it would be useful to quantitatively explore the parameter space for this model, to see how well constrained are the temperature and optical depth (expressed in y) for this model. Furthermore, investigating how sensitive our results are to the surface luminosity we use may give us an insight into how applicable this model might be to other sources, with different burst behaviours.

CHAPTER 4
Conclusion

In this work, we have shown that with a simple model for spreading, we were able to be very closely reproduce both flux and spectral observations in the early parts of bursts from GS 1826-24. We also showed that with a very simple model for Comptonization of a blackbody spectrum, we were able to reproduce, and thus provide a possible explanation for, the observed decreasing inferred emission area in the tails of bursts from this same source.

In the future, it would be interesting to test our models, as well as the assertions made based on the study of this source, to other type I X-ray burst sources.

Improving our model to include ignition away from the equator, as well as burst fronts which spread as growing *hot spots* would allow us to undertand what effects the different ignition regimes may have on lightcurves and burst spectra, and to eventually test the associated theoretical predictions by comparing to observations.

APPENDIX A
Analytical calculation of belt-like burst as seen from the pole and from the equator

In this section, we attempt to compute the luminosity of a burst resorting to analytical methods only. Starting with a general expression for an arbitrary direction of observation $\boldsymbol{p}$

$$dL = FdS(\boldsymbol{p} \cdot \boldsymbol{r}) \tag{A.1}$$

The flux F will be defined as follows:

$$F(t, \phi, \theta) = \begin{cases} 0 & \text{if } \pi/2 - \theta > \omega t \\ F_0 e^{-\frac{(t - t_s(1 - \frac{2\theta}{\pi}))}{\tau}} & \text{if } \pi/2 - \theta < \omega t \end{cases} \tag{A.2}$$

where θ is the polar angle in spherical coordinates, τ is the timescale corresponding to the exponential fall of the burst and $\omega = \pi/2t_s$ is the angular speed of the burst front. Precisely, it is the time it takes for the flux from a given point on the star, from the moment it has ignited, to reach $1/e$ of its initial amplitude. t_s is the time it takes for the burst-front to travel from the equator to the pole and is thus defined as

$$t_s = \frac{\pi}{2\omega} = \frac{\pi R}{2v} \tag{A.3}$$

where v is the linear speed of the burst front and R is the radius of the star.

Now we can begin to treat the special cases where $\boldsymbol{p}$ is on the equator or on the poles. Let's start with the latter, letting $\boldsymbol{p} = \hat{z}$ and thus the integral in equation A.1 becomes

$$L(t) = \int_{\frac{\pi}{2} - \frac{\pi t}{2t_s}}^{\frac{\pi}{2}} d\theta \int_0^{2\pi} d\phi R^2 \sin\theta \cos\theta F_0 e^{-\frac{(t - t_s(1 - \frac{2\theta}{\pi}))}{\tau}} \tag{A.4}$$

Given the restriction $0 \leq \theta \leq \pi$, we need to modify the lower limit of the integral with respect to θ for times $t > t_s$, effectively halting the propagation once the front has reached the pole. The expression for the luminosity then becomes

$$L(t) = \begin{cases} \int_{\frac{\pi}{2}-\frac{\pi t}{2t_s}}^{\frac{\pi}{2}} d\theta \int_0^{2\pi} d\phi R^2 \sin\theta\cos\theta F_0 e^{-\frac{(t-t_s(1-\frac{2\theta}{\pi}))}{\tau}} & \text{for } 0 \leq t \leq t_s \\ \int_0^{\frac{\pi}{2}} d\theta \int_0^{2\pi} d\phi R^2 \sin\theta\cos\theta F_0 e^{-\frac{(t-t_s(1-\frac{2\theta}{\pi}))}{\tau}} & \text{for } t > t_s \end{cases} \tag{A.5}$$

which, once integrated, yields the following:

$$L(t) = \begin{cases} \frac{\tau F_0 R^2 \pi^2}{2(t_s^2+\pi^2\tau^2)} \left[-\pi\tau\cos(\frac{\pi t}{t_s}) + t_s \sin(\frac{\pi t}{t_s}) + \pi\tau e^{-\frac{t}{\tau}}\right] & \text{for } 0 \leq t \leq t_s \\ \frac{\tau^2 F_0 R^2 \pi^3}{2(t_s^2+\pi^2\tau^2)} \left(e^{\frac{t_s}{\tau}} + 1\right) e^{-\frac{t}{\tau}} & \text{for } t > t_s \end{cases} \tag{A.6}$$

Now onto the case where the observation direction vector $\boldsymbol{p}$ is on the equator. Let $\boldsymbol{p} = \hat{x}$. Equation A.1 becomes

$$L(t) = \begin{cases} 2\int_{\frac{\pi}{2}-\frac{\pi t}{2t_s}}^{\frac{\pi}{2}} d\theta \int_{-\pi/2}^{\pi/2} d\phi R^2 \sin^2\theta\cos\phi F_0 e^{-\frac{(t-t_s(1-\frac{2\theta}{\pi}))}{\tau}} & \text{for } 0 \leq t \leq t_s \\ 2\int_0^{\frac{\pi}{2}} d\theta \int_{-\pi/2}^{\pi/2} d\phi R^2 \sin^2\theta\cos\phi F_0 e^{-\frac{(t-t_s(1-\frac{2\theta}{\pi}))}{\tau}} & \text{for } t > t_s \end{cases} \tag{A.7}$$

which after integration yields

$$I(t) = \begin{cases} \frac{\tau F_0 R^2 \pi}{t_s(t_s^2+\pi^2\tau^2)} \left[t_s^2 + \pi^2\tau^2 + t_s^2\cos(\frac{\pi t}{t_s}) + \pi t_s \tau \sin(\frac{\pi t}{t_s}) - (2t_s^2+\pi^2\tau^2)e^{-\frac{t}{\tau}}\right] & \text{for } 0 \leq t \leq t_s \\ \frac{\tau F_0 R^2 \pi}{t_s(t_s^2+\pi^2\tau^2)} \left(\pi^2\tau^2 e^{\frac{t_s}{\tau}} - 2t_s^2 - \pi^2\tau^2\right) e^{-\frac{t}{\tau}} & \text{for } t > t_s \end{cases} \tag{A.8}$$

Setting $R = \tau = t_s = F_0 = 1$, we can generate two lightcurves for the bursts as seen from the pole (in red) and from the equator (in green), in Figure A–1.

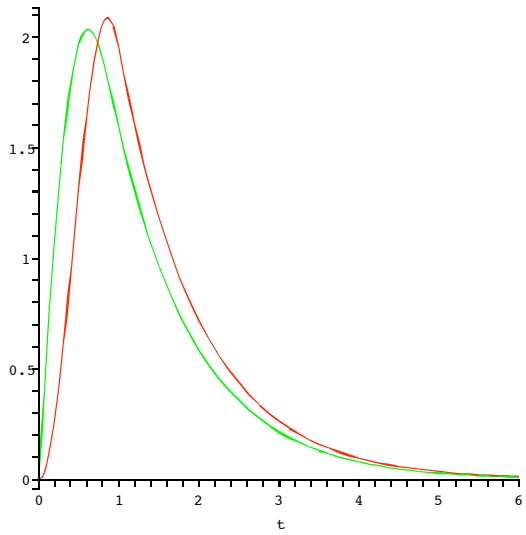

Figure A–1: Luminosity of a burst with equatorial ignition viewed from the equator (green) and the pole (red)

APPENDIX B
Bayesian statistics

The two important tools we utilized are *Bayes' theorem* and the principle of *marginalisation*:

$$\mathrm{P}(A|B) \;=\; \frac{\mathrm{P}(B|A)\,\mathrm{P}(A)}{\mathrm{P}(B)} \tag{B.1}$$

and

$$\mathrm{P}(X) \;=\; \int_{-\infty}^{+\infty} \mathrm{P}(X,Y)\,dY \tag{B.2}$$

respectively. Replacing A and B by *data* and *model*, we can rewrite equation (B.1) as

$$\mathrm{P}(\mathit{model}|\mathit{data}) \;\propto\; \mathrm{P}(\mathit{data}|\mathit{model})\,\mathrm{P}(\mathit{model}) \tag{B.3}$$

where we have omitted the denominator $\mathrm{P}(B)$ from equation (B.1), which is fine as it doesn't depend explicitly on the model, and thus simply serves as a normalisation constant. $\mathrm{P}(\mathit{model}|\mathit{data})$ is called the *posterior* probability, $\mathrm{P}(\mathit{data}|\mathit{model})$ the *likelihood function* and $\mathrm{P}(\mathit{model})$ is the *prior*. The prior represents our knowledge of the likelihood of the model before having analysed the data. The posterior function is what we are looking for, as it tells us how likely it is that our proposed model is acceptable, given a data set (observations).

Assuming that each point in the data set was measured independently, we can rewrite the likelihood function $\mathrm{P}(\mathit{data}|\mathit{model})$ as a product of the

probabilities for the individual measurements (d_i):

$$\mathrm{P}(data|model) \;=\; \mathrm{P}(d_1, d_2, d_3..., d_N|model) \;=\; \prod_{i=1}^{N} \mathrm{P}(d_i|model) \qquad \text{(B.4)}$$

If we also assume that the error associated with each experimental measurement can be represented by a Gaussian distribution, then the probability of an individual measurement d_i with error σ_i given a prediction from the model of m_i is

$$\mathrm{P}(d_i|model) \;=\; \frac{1}{\sigma_i\sqrt{2\pi}} \exp\left(-\frac{(m_i - d_i)^2}{2\sigma_i^2}\right) \qquad \text{(B.5)}$$

We can now write the likelihood function as

$$\mathrm{P}(data|model) \;\propto\; \prod_{i=1}^{N} \exp\left(-\frac{(m_i - d_i)^2}{2\sigma_i^2}\right) \qquad \text{(B.6)}$$

or

$$\mathrm{P}(data|model) \;\propto\; \exp\left(-\frac{1}{2}\sum_{i=1}^{N} \frac{(m_i - d_i)^2}{\sigma_i^2}\right) \qquad \text{(B.7)}$$

By recognizing the expression inside the exponential as being proportional to the χ^2 sum, the expression finally simplifies to

$$\mathrm{P}(data|model) \;\propto\; \exp\left(-\chi^2/2\right) \qquad \text{(B.8)}$$

We can now assign a probability to each model by rewriting equation (B.3) using (B.2) and (B.8).

Our models depend on the 3 parameters t_s, i and z. Assuming we wanted to find a probability distribution as a function of one of the model parameters, say t_s, we would have to evaluate

$$\mathrm{P}(model(t_s)|data) \;\propto\; \int dz' \int di' \, \exp\left(-\frac{\chi^2(t_s, i', z')}{2}\right) \mathrm{P}(model) \qquad \text{(B.9)}$$

with an appropriately chosen prior $\mathrm{P}(model)$.

References

W. Baade and F. Zwicky. Remarks on super-novae and cosmic rays. *Phys. Rev.*, 46(1):76–77, Jul 1934. doi: 10.1103/PhysRev.46.76.2.

D. Barret, J. F. Olive, L. Boirin, C. Done, G. K. Skinner, and J. E. Grindlay. Hard X-Ray Emission from Low-Mass X-Ray Binaries. *ApJ*, 533: 329–351, April 2000. doi: 10.1086/308651.

A. M. Beloborodov. Gravitational Bending of Light Near Compact Objects. *ApJ*, 566:L85–L88, February 2002. doi: 10.1086/339511.

L. Bildsten. Thermonuclear Burning on Rapidly Accreting Neutron Stars. In R. Buccheri, J. van Paradijs, & A. Alpar, editor, *NATO ASIC Proc. 515: The Many Faces of Neutron Stars.*, pages 419–+, 1998.

L. Bildsten. Theory and observations of Type I X-Ray bursts from neutron stars. In S. S. Holt & W. W. Zhang, editor, *American Institute of Physics Conference Series*, volume 522 of *American Institute of Physics Conference Series*, pages 359–369, June 2000. doi: 10.1063/1.1291736.

S. Boutloukos, M. C. Miller, and F. K. Lamb. Super-Eddington fluxes during thermonuclear X-ray bursts. *ArXiv e-prints*, March 2010.

J. S. Chang and G. Cooper. A Practical Difference Scheme for Fokker-Planck Equations. *Journal of Computational Physics*, 6:1–+, August 1970. doi: 10.1016/0021-9991(70)90001-X.

J. F. Chen and J. H. You. Diffusion approximation in the theory of radiative transfer. *Ap&SS*, 199:19–22, January 1993. doi: 10.1007/BF00612973.

D. D. Clayton. *Principles of stellar evolution and nucleosynthesis.* 1968.

M. Cocchi, R. Farinelli, A. Paizis, and L. Titarchuk. Wide band observations of the X-ray burster GS 1826-238. *A&A*, 509:A2+, January 2010. doi: 10.1051/0004-6361/200912796.

R. L. Cooper and R. Narayan. A Two-Zone Model for Type I X-Ray Bursts on Accreting Neutron Stars. *ApJ*, 652:584–596, November 2006. doi: 10.1086/507782.

R. L. Cooper and R. Narayan. The Latitude of Type I X-Ray Burst Ignition on Rapidly Rotating Neutron Stars. *ApJ*, 657:L29–L32, March 2007. doi: 10.1086/513077.

A. Cumming. Thermonuclear X-ray bursts: theory vs. observations. *Nuclear Physics B Proceedings Supplements*, 132:435–445, June 2004. doi: 10.1016/j.nuclphysbps.2004.04.078.

S. del Sordo, F. Frontera, E. Pian, S. Piraino, T. Oosterbroek, B. A. Harmon, E. Palazzi, M. Tavani, S. N. Zhang, and A. N. Parmar. BeppoSAX Observations of the Galactic Source GS 1826-238 in a Hard X-Ray High State. *Astrophysical Letters Communications*, 38:125–+, 1999.

J. Frank, A. R. King, and D. J. Raine. *Accretion power in astrophysics*. 1985.

D. K. Galloway, A. Cumming, E. Kuulkers, L. Bildsten, D. Chakrabarty, and R. E. Rothschild. Periodic Thermonuclear X-Ray Bursts from GS 1826-24 and the Fuel Composition as a Function of Accretion Rate. *ApJ*, 601:466–473, January 2004. doi: 10.1086/380445.

D. K. Galloway, M. P. Muno, J. M. Hartman, D. Psaltis, and D. Chakrabarty. Thermonuclear (Type I) X-Ray Bursts Observed by the Rossi X-Ray Timing Explorer. *ApJS*, 179:360–422, December 2008. doi: 10.1086/592044.

C. J. Hansen, S. D. Kawaler, and V. Trimble. *Stellar interiors : physical principles, structure, and evolution*. 2004.

A. Heger, A. Cumming, D. K. Galloway, and S. E. Woosley. Models of Type I X-Ray Bursts from GS 1826-24: A Probe of rp-Process Hydrogen Burning. *ApJ*, 671:L141–L144, December 2007. doi: 10.1086/525522.

J. W. T. Hessels, S. M. Ransom, I. H. Stairs, P. C. C. Freire, V. M. Kaspi, and F. Camilo. A Radio Pulsar Spinning at 716 Hz. *Science*, 311: 1901–1904, March 2006. doi: 10.1126/science.1123430.

L. Homer, P. A. Charles, and D. O'Donoghue. Evidence for a 2-h optical modulation in GS 1826-24. *MNRAS*, 298:497–501, August 1998. doi: 10.1046/j.1365-8711.1998.01656.x.

F. Hoyle. On Nuclear Reactions Occuring in Very Hot STARS.I. the Synthesis of Elements from Carbon to Nickel. *ApJS*, 1:121–+, September 1954. doi: 10.1086/190005.

J. J. M. in 't Zand, J. Heise, E. Kuulkers, A. Bazzano, M. Cocchi, and P. Ubertini. Broad-band X-ray measurements of GS 1826-238. *A&A*, 347: 891–896, July 1999.

J. J. M. in't Zand, L. Keek, A. Cumming, A. Heger, J. Homan, and M. Méndez. Long tails on thermonuclear X-ray bursts from neutron stars: a signature of inward heating? *A&A*, 497:469–480, April 2009. doi: 10.1051/0004-6361/200811432.

J. M. Lattimer and M. Prakash. Neutron Star Structure and the Equation of State. *ApJ*, 550:426–442, March 2001. doi: 10.1086/319702.

W. H. G. Lewin, J. van Paradijs, and R. E. Taam. X-Ray Bursts. *Space Science Reviews*, 62:223–389, September 1993. doi: 10.1007/BF00196124.

Q. Z. Liu, J. van Paradijs, and E. P. J. van den Heuvel. A catalogue of low-mass X-ray binaries in the Galaxy, LMC, and SMC (Fourth edition).

A&A, 469:807–810, July 2007. doi: 10.1051/0004-6361:20077303.

R. A. London, W. M. Howard, and R. E. Taam. The spectra of X-ray bursting neutron stars. *ApJ*, 287:L27–L30, December 1984. doi: 10.1086/184390.

R. A. London, R. E. Taam, and W. M. Howard. Model atmospheres for X-ray bursting neutron stars. *ApJ*, 306:170–182, July 1986. doi: 10.1086/164330.

J. Madej, P. C. Joss, and A. Różańska. Model Atmospheres and X-Ray Spectra of Bursting Neutron Stars: Hydrogen-Helium Comptonized Spectra. *ApJ*, 602:904–912, February 2004. doi: 10.1086/379761.

A. Majczyna, J. Madej, P. C. Joss, and A. Różańska. Model atmospheres and X-ray spectra of bursting neutron stars. II. Iron rich comptonized spectra. *A&A*, 430:643–654, February 2005. doi: 10.1051/0004-6361:20034048.

N. Nakamura, T. Dotani, H. Inoue, K. Mitsuda, Y. Tanaka, and M. Matsuoka. TENMA observation of X-ray bursts from X1608-52. *PASJ*, 41: 617–639, 1989.

J. Nishimura, K. Mitsuda, and M. Itoh. Comptonization of soft X-ray photons in an optically thin hot plasma. *PASJ*, 38:819–830, 1986.

J. C. B. Papaloizou and D. N. C. Lin. Theory Of Accretion Disks I: Angular Momentum Transport Processes. *ARA&A*, 33:505–540, 1995. doi: 10.1146/annurev.aa.33.090195.002445.

G. B. Rybicki and A. P. Lightman. *Radiative processes in astrophysics*. 1979.

H. Schatz, A. Aprahamian, V. Barnard, L. Bildsten, A. Cumming, M. Ouellette, T. Rauscher, F.-K. Thielemann, and M. Wiescher. End Point of the rp Process on Accreting Neutron Stars. *Physical Review Letters*, 86:

3471–3474, April 2001. doi: 10.1103/PhysRevLett.86.3471.

M. Schwarzschild and R. Härm. Therma Instability in Non-Degenerate Stars. *ApJ*, 142:855–+, October 1965. doi: 10.1086/148358.

M. M. Shara. Localized thermonuclear runaways and volcanoes on degenerate dwarf stars. *ApJ*, 261:649–660, October 1982. doi: 10.1086/160376.

K. Smith, A. M. Amthor, R. Cyburt, A. Heger, E. Johnson, and H. Schatz. Sensitivity of X-ray Burst Models to Uncertainties in Nuclear Processes. *APS Meeting Abstracts*, pages F6+, October 2008.

A. Spitkovsky, Y. Levin, and G. Ushomirsky. Propagation of Thermonuclear Flames on Rapidly Rotating Neutron Stars: Extreme Weather during Type I X-Ray Bursts. *ApJ*, 566:1018–1038, February 2002. doi: 10.1086/338040.

M. Strickman, J. Skibo, W. Purcell, D. Barret, and C. Motch. OSSE detection of the low mass X-ray binary GS 1826-24. *A&AS*, 120:C217+, December 1996.

T. E. Strohmayer, W. Zhang, and J. H. Swank. 363 HZ Oscillations during the Rising Phase of Bursts from 4U 1728-34: Evidence for Rotational Modulation. *ApJ*, 487:L77+, September 1997. doi: 10.1086/310880.

V. Suleimanov, J. Poutanen, M. Revnivtsev, and K. Werner. Neutron star stiff equation of state derived from cooling phases of the X-ray burster 4U 1724-307. *ArXiv e-prints*, April 2010.

Y. Tanaka. Black holes in X ray binaries: X ray properties of the galactic black hole candidates. In J. Hunt & B. Battrick, editor, *Two Topics in X-Ray Astronomy, Volume 1: X Ray Binaries. Volume 2: AGN and the X Ray Background*, volume 296 of *ESA Special Publication*, pages 3–13, November 1989.

T. M. Tauris and E. van den Heuvel. Formation and Evolution of Compact Stellar X-ray Sources. *ArXiv Astrophysics e-prints*, March 2003.

T. W. J. Thompson, R. E. Rothschild, J. A. Tomsick, and H. L. Marshall. Chandra and RXTE Spectra of the Burster GS 1826-238. *ApJ*, 634: 1261–1271, December 2005. doi: 10.1086/497104.

S. E. Thorsett and D. Chakrabarty. Neutron Star Mass Measurements. I. Radio Pulsars. *ApJ*, 512:288–299, February 1999. doi: 10.1086/306742.

P. Ubertini, A. Bazzano, M. Cocchi, L. Natalucci, J. Heise, R. Jager, J. in 't Zand, J. M. Muller, M. Smith, G. Celidonio, A. Coletta, R. Ricci, P. Giommi, D. Ricci, M. Capalbi, M. T. Menna, and S. Rebecchi. GS 1826-238. *IAU Circ.*, 6611:1–+, April 1997.

P. Ubertini, A. Bazzano, M. Cocchi, L. Natalucci, J. Heise, J. M. Muller, and J. J. M. in 't Zand. Bursts from GS 1826-238: A Clocked Thermonuclear Flashes Generator. *ApJ*, 514:L27–L30, March 1999. doi: 10.1086/311933.

J. van Paradijs and H. G. Lewin. The interpretation of blackbody spectra and radii during X-ray bursts. *A&A*, 157:L10–L12, March 1986.

M. Wiescher, J. Grres, E. Uberseder, G. Imbriani, and M. Pignatari. The cold and hot cno cycles. *Annual Review of Nuclear and Particle Science*, 60(1), 2010. doi: 10.1146/annurev.nucl.012809.104505. URL `https://www.annualreviews.orghttps://www.annualreviews.org/doi/abs/10.1146/annur`

S. E. Woosley, A. Heger, and T. A. Weaver. The evolution and explosion of massive stars. *Reviews of Modern Physics*, 74:1015–1071, November 2002. doi: 10.1103/RevModPhys.74.1015.

S. E. Woosley, A. Heger, A. Cumming, R. D. Hoffman, J. Pruet, T. Rauscher, J. L. Fisker, H. Schatz, B. A. Brown, and M. Wiescher. Models for Type I X-Ray Bursts with Improved Nuclear Physics. *ApJS*,

151:75–102, March 2004. doi: 10.1086/381533.